

# X-ray scaling relations from a complete sample of the richest maxBCG clusters

Chong Ge<sup>1\*</sup>, Andrea Morandi<sup>1</sup>, Ming Sun<sup>1†</sup>, Eduardo Rozo<sup>2</sup>, Neelima Sehgal<sup>3</sup>, Alexey Vikhlinin<sup>4</sup>, William Forman<sup>4</sup>, Christine Jones<sup>4</sup>, and Daisuke Nagai<sup>5,6,7</sup>

<sup>1</sup>Physics Department, University of Alabama in Huntsville, Huntsville, AL 35899, USA

<sup>2</sup>Department of Physics, University of Arizona, Tucson, AZ 85721, USA

<sup>3</sup>Physics and Astronomy Department, Stony Brook University, Stony Brook, NY 11794, USA

<sup>4</sup>Harvard-Smithsonian Center for Astrophysics, 60 Garden Street, Cambridge, MA 02138, USA

<sup>5</sup>Department of Physics, Yale University, New Haven, CT 06520, USA

<sup>6</sup>Department of Astronomy, Yale University, New Haven, CT 06520, USA

<sup>7</sup>Yale Center for Astronomy & Astrophysics, Yale University, New Haven, CT 06520, USA

Accepted. Received; in original form

## ABSTRACT

The galaxy cluster scaling relations are important for studying baryon physics, structure formation and cosmology. We use a complete sample of 38 richest maxBCG clusters to study the ICM-galaxy scaling relations based on X-ray and optical observations. The clusters are selected from the two largest bins of optical richness in the *Planck* stacking work with the maxBCG richness  $N_{200} \geq 78$ . We analyze their *Chandra* and *XMM-Newton* data to derive the X-ray properties of the ICM. While the expected cluster temperatures should be scattered around 5 - 10 keV from the optical richness, the observed range extends to temperatures as low as 1.5 keV. Meanwhile, they follow normal  $L_X - T_X$  and  $L_X - Y_X$  relations, which suggests that they are normal X-ray clusters. Moreover, the observed average  $Y_X$  is consistent with the expected  $Y_X$  inferred from the *Planck* mean stacking  $Y_{SZ}$  in the same two richest bins. However, the scatter of the  $L_X - N$  and  $Y_X - N$  relations are also large and asymmetric with more outliers towards lower  $L_X$  or  $Y_X$ . The mismatch between ICM-galaxy scaling relations can come from several factors, including miscentering, projection, contamination of low mass systems, mass bias and covariance bias. The mismatch is smaller when using a BCG-dominated subsample, with the outliers suffering from the projection problem. Our results suggest that results from blind stacking should be interpreted carefully. We also evaluate the fractions of relaxed and cool core (CC) clusters in our sample. Both are smaller than those from SZ or X-ray selected samples.

**Key words:** galaxies: clusters: general – galaxies: clusters: intracluster medium – X-rays: galaxies: clusters.

## 1 INTRODUCTION

Galaxy clusters are excellent cosmology probes as they are the largest virialized structures in the Universe. Their spatial distribution and number density are very sensitive to the underlying cosmological parameters. They have been used to study cosmology for over twenty years (e.g., Henry & Arnaud 1991; Eke et al. 1998; Reiprich & Böhringer 2002; Vikhlinin et al. 2009b; Rozo et al. 2010; Sehgal et al. 2011; Allen et al. 2011). The key questions to study cosmology

with clusters are how to find clusters and how to measure their masses. While the cluster mass can be measured by lensing and the velocity dispersion of cluster galaxies, both of them are observationally expensive. They are not efficient methods for finding clusters, though they are important tools for direct mass calibration. These measurements find that most cluster mass is in dark matter, which cannot be detected directly, thus more conveniently the cluster finding and mass measuring are tied to baryons in clusters.

A small fraction of cluster baryons cooled and formed stars. Clusters can be selected optically by looking for overdense regions of galaxies. The optical identifications have resulted in large samples of clusters, benefiting from large

\* chong.ge@uah.edu

† ming.sun@uah.edu

optical surveys like *SDSS* (e.g., Koester et al. 2007; Rykoff et al. 2014). Mass proxies in optical are generally the total number or luminosity of member galaxies but such scaling relations suffer from large scatters.

Most of the cluster baryons are in the hot intracluster medium (ICM). The ICM emits X-rays via thermal bremsstrahlung and line emission, which are proportional to the density square of the gas that traces the deep potential well of the cluster. Thus, the X-ray detection is very effective to find clusters and relatively free from projection contamination. Meanwhile, the cluster mass can be derived from the distribution of their X-ray emitting gas under the assumption of hydrostatic equilibrium (HE). A more economical way is using X-ray mass proxies like  $T_X$ ,  $L_X$  and  $Y_X$  through scaling relations (e.g., Kaiser 1986; Pratt et al. 2009; Vikhlinin et al. 2009a; Sun et al. 2009; Mantz et al. 2010; Sun et al. 2011; Sun 2012). These X-ray mass proxies, usually considered robust and low scattered, can also be calibrated with the robust mass indicators like weak lensing mass. The ICM scaling relations are also important to understand the key baryon physics that governs galaxy formation, e.g., cooling, efficiency of star formation (e.g., Kravtsov et al. 2005), and stellar or AGN feedback (e.g., Croton et al. 2006; Bower et al. 2008).

The X-ray emitting hot electrons also boost microwave background radiation (CMB) photons to higher energy through inverse Compton scattering (Sunyaev-Zel'dovich — SZ effect; Carlstrom et al. 2002). The SZ signal, which is proportional to gas density and temperature, is a promising way to find clusters and complementary to X-ray measurements. Tremendous progress has been made in the past ten years with the SZ surveys from *Planck*, the Atacama Cosmology Telescope (*ACT*), and the South Pole Telescope (*SPT*). Hundreds of new clusters have been discovered (e.g., Planck Collaboration et al. 2016). Scaling relations between the SZ observables and the other observables in X-ray and optical have been established (e.g., Planck Collaboration et al. 2011c). The total SZ flux has been considered a robust mass proxy, as it measures the total thermal energy of the ICM. However, the new SZ data have also raised new puzzles. One that has received much attention is the mismatch between the stacked *Planck* SZ fluxes and the model expectations for the optically selected clusters. All the model SZ fluxes from optically selected clusters overpredict the observed SZ fluxes from *Planck* (Planck Collaboration et al. 2011d), *ACT* (Sehgal et al. 2013), and *SPT* (Saro et al. 2017). Possible solutions include: 1) the impurity of the optically selected sample; 2) miscentering because of the offset between the optical center and the ICM peak; 3) contamination of optical richness estimates from line-of-sight projections; 4) contamination of the SZ flux from radio galaxies, infrared galaxies, Galactic emission, and the SZ background from unresolved clusters, groups, and the intergalactic medium; 5) underestimate of the true mass by the X-ray HE mass because of additional non-thermal pressure from e.g., gas bulk motion and turbulence; 6) Eddington bias and X-ray selection bias (e.g., Rykoff et al. 2008; Planck Collaboration et al. 2011d; Biesiadzinski et al. 2012; Sehgal et al. 2013; Rozo et al. 2014b; Saro et al. 2017).

While the previous studies addressing this puzzle require the calibration of the true mass and assume pressure templates, we bypass this intermediate step to directly com-

pare the X-ray properties with the optical richness, which further allows a direct comparison of the pressure content from X-rays and SZ in the future. We target the most massive maxBCG clusters as the mismatch exists in all richness bins. These clusters should have the strongest X-ray and SZ signals. It is natural to study them directly to examine the reasons for the mismatch. There are 38 clusters in the two richest bins (Fig. 1 in Planck Collaboration et al. 2011d and Table 1). When we first started this project, 31 of them had existing *Chandra* or *XMM* data, and were mostly X-ray selected. The remaining seven clusters are generally X-ray faint from the *ROSAT* All Sky Survey (RASS). We proposed new *XMM* observations (proposal id 74251 and 76159, PI: Sun) on these seven clusters (shown in Table 2) to have full X-ray coverage of this sample. In addition to the maxBCG catalogue, we also use the redMaPPer catalogue (Rykoff et al. 2014) as a complementary study.

We organise the paper as follows: Section 2 includes the cluster sample and catalogues; Section 3 details our X-ray data reduction and analysis; Section 4 presents results based on X-ray data and optical catalogues; Section 5 is the discussion; and Section 6 is our conclusions. We use the standard cold dark matter cosmology with  $H_0 = 70 \text{ km s}^{-1} \text{ Mpc}^{-1}$ ,  $\Omega_m = 0.3$ , and  $\Omega_\Lambda = 0.7$ .

## 2 CLUSTER SAMPLE

Table 1 lists the 38 richest maxBCG clusters with optical and SZ properties assembled from maxBCG, redMaPPer, and PSZ2 catalogues, which are introduced briefly below. We use  $N$  as a general representative of optical richness, particularly  $N_{200}$  for maxBCG and  $\lambda$  for redMaPPer.

### 2.1 maxBCG catalogue

The maxBCG cluster catalogue (Koester et al. 2007) contains 13823 clusters selected from *SDSS* Data Release 5 (DR5), with photometric redshifts of 0.1–0.3 over approximately volume-limited 7500 deg<sup>2</sup> of sky. Each cluster is selected as a spatial overdensity of red-sequence galaxies that form a tight E/S0 ridgeline in the color-magnitude diagram. The cluster center is on the brightest cluster galaxy (BCG) with the highest likelihood. The tight relation between the ridgeline color and redshift also provides an accurate photometric redshift estimate for each cluster ( $\Delta_z \simeq 0.01$ ). The cluster richness  $N_{200}$  is defined as the number of red-sequence galaxies with rest-frame i-band luminosity  $L_i > 0.4L_*$  within a projected scaled radius  $R_{200}$ , interior to which the density of galaxies with  $-24 < M_r < -16$  is 200 times the mean density of such kind of galaxies. Applying the cluster selection algorithm to mock catalogues suggests that the catalogue is  $\sim 90\%$  pure and  $\sim 85\%$  complete for clusters with masses  $\geq 10^{14} M_\odot$ . The maxBCG cluster mass has been calibrated by Rozo et al. (2009) with the  $M_{500c} - N_{200}$  relation.

### 2.2 redMaPPer catalogue

The redMaPPer cluster catalogue (v6.3; Rykoff et al. 2014) includes 26111 clusters identified from *SDSS* DR8, with photometric redshifts of 0.08–0.60 (volume-limited in  $z \leq 0.35$ ),

**Table 1.** Optical and SZ properties of the richest maxBCG clusters

Cluster	RA <sup>a</sup>	DEC <sup>a</sup>	$z_{\text{photo}}^a$	$N_{200}^a$	redMaPPer <sup>b</sup> RM	$\lambda^b$	offset <sup>b</sup> arcmin	Planck <sup>c</sup> PSZ2	SNR <sup>c</sup>	offset <sup>c</sup> arcmin
A2142	239.58334	27.23342	0.103	188	J155820.0+271400.3	$169.8 \pm 4.2$	0.00	G044.20+48.66	28.4	1.56
J150	150.68705	20.49151	0.297	164	J100214.1+203216.6	$151.4 \pm 5.8$	7.72	G213.30+50.99	4.5	3.91
					J100311.3+203230.2	$54.7 \pm 4.4$	6.88			
A1689	197.87292	-1.34110	0.189	156	J131129.5-012028.0	$164.7 \pm 4.2$	0.00	G313.33+61.13	16.7	0.81
A1443	180.31985	23.10909	0.262	139	J120112.2+230557.3	$131.3 \pm 5.9$	1.20	G229.74+77.96	12.0	0.87
A781	140.10742	30.49406	0.292	126	J092052.5+302740.3	$128.6 \pm 5.7$	6.09	G195.60+44.06	7.6	0.72
					J092030.0+302946.8	$38.7 \pm 5.2$	0.92			
A1986	223.37531	21.87434	0.116	120	J145308.4+215339.3	$68.8 \pm 3.2$	5.18	-	-	-
A1882	213.78496	-0.49325	0.135	115	J141424.1-002239.5	$105.1 \pm 3.8$	13.07	-	-	-
A1758	203.16008	50.55992	0.284	114	J133238.4+503336.0	$152.9 \pm 5.7$	0.00	G107.10+65.32	16.5	2.59
					J133224.5+502425.8	$51.9 \pm 4.2$	9.43			
A1760	203.53616	20.24806	0.176	113	J133431.5+201217.7	$73.4 \pm 3.7$	5.94	G000.13+78.04	9.3	1.35
					J133359.1+201801.3	$26.5 \pm 3.7$	3.85			
A1622	192.38517	49.89549	0.275	107	J124922.1+494742.1	$129.3 \pm 5.6$	6.25	G123.66+67.25	5.7	2.02
A750	137.21745	11.02649	0.173	107	J090912.2+105824.9	$174.7 \pm 4.9$	5.84	G218.81+35.51	8.4	4.84
A1682	196.69040	46.55854	0.235	106	J130650.0+463333.4	$122.4 \pm 5.3$	0.74	G114.99+70.36	10.0	2.52
A1246	171.01653	21.49114	0.186	103	J112358.8+212849.7	$113.6 \pm 4.1$	1.36	G224.00+69.33	8.8	0.67
A1961	221.07852	31.28601	0.240	101	J144431.8+311336.0	$114.8 \pm 4.6$	4.51	G049.18+65.05	6.1	3.79
A2034	227.54883	33.48646	0.122	99	J151011.7+332911.3	$99.8 \pm 3.7$	0.00	G053.53+59.52	15.9	0.42
A655	126.37104	47.13348	0.135	99	J082529.1+470800.9	$131.6 \pm 4.8$	0.01	G172.63+35.15	7.4	1.19
A1914	216.48612	37.81645	0.167	98	J142556.7+374859.2	$103.3 \pm 4.0$	0.00	G067.17+67.46	17.8	0.81
Z5247	188.57278	9.76624	0.243	98	J123424.1+094715.5	$93.0 \pm 4.2$	2.08	G289.13+72.19	8.8	2.71
A657	125.83033	15.96272	0.157	94	J082319.3+155745.8	$82.1 \pm 3.9$	0.00	-	-	-
J229	229.35068	-0.73816	0.119	93	J151721.9-004256.3	$58.1 \pm 3.0$	1.47	-	-	-
A1423	179.32219	33.61093	0.219	91	J115715.2+333638.5	$86.0 \pm 4.2$	0.45	G180.60+76.65	11.0	0.56
A801	142.01889	20.52921	0.208	91	J092804.5+203145.1	$93.0 \pm 4.5$	0.00	G209.53+43.32	4.8	2.32
A773	139.47261	51.72704	0.224	90	J091753.4+514337.5	$153.6 \pm 4.7$	0.00	G166.09+43.38	12.4	0.51
A1576	189.24684	63.18658	0.294	89	J123658.6+631114.1	$102.6 \pm 4.8$	0.08	G125.71+53.86	11.4	0.60
A2631	354.41554	0.27138	0.286	88	J233739.7+001616.9	$126.3 \pm 4.9$	0.00	G087.03-57.37	11.2	1.00
A1703	198.77182	51.81738	0.286	87	J131505.2+514902.8	$152.5 \pm 4.9$	0.00	G114.31+64.89	11.1	0.96
A2219	250.08254	46.71148	0.235	85	J164019.8+464241.5	$199.5 \pm 5.3$	0.00	G072.62+41.46	27.4	0.48
A1319	174.05437	40.04327	0.292	85	J113613.0+400235.8	$155.1 \pm 5.9$	0.00	G168.33+69.73	5.6	3.60
A1560	188.47087	15.19464	0.275	84	J123416.1+151508.4	$136.9 \pm 6.1$	6.57	G283.26+77.37	6.0	1.53
J175	175.57289	10.29192	0.127	84	J114200.5+102422.2	$44.8 \pm 4.0$	8.03	-	-	-
					J114207.4+100857.6	$38.4 \pm 2.6$	8.91			
J249	249.89850	47.07569	0.227	84	J163938.0+470310.4	$61.8 \pm 3.4$	1.43	-	-	-
A1201	168.22709	13.43584	0.176	83	J111250.1+132830.4	$78.3 \pm 3.5$	2.59	G238.69+63.26	7.3	3.01
A2009	225.08133	21.36941	0.165	82	J150019.5+212209.9	$91.8 \pm 3.6$	0.00	G028.89+60.13	7.5	0.79
A2111	234.91872	34.42425	0.243	81	J153940.5+342527.3	$151.5 \pm 5.2$	0.00	G054.99+53.41	8.4	0.94
A815	143.03590	29.06782	0.281	80	J093208.6+290404.1	$92.2 \pm 5.9$	0.00	-	-	-
Z1450	223.05481	37.87803	0.284	79	J145213.1+375251.9	$101.9 \pm 4.5$	0.18	-	-	-
A1765	204.20577	10.44002	0.159	78	J133649.4+102624.1	$82.7 \pm 3.7$	0.00	-	-	-
A1902	215.41700	37.29131	0.165	78	J142140.1+371728.7	$82.5 \pm 3.8$	0.00	G066.68+68.44	7.1	0.90

Note. <sup>a</sup>: From maxBCG catalogue (Koester et al. 2007); RA and DEC mark the cluster center defined as the BCG location;  $z_{\text{photo}}$  is the photometric redshift;  $N_{200}$  is the maxBCG richness given by the number of E/S0 ridgeline galaxies more luminous than  $0.4L^*$  within a scaled radius  $R_{200}$ . <sup>b</sup>: From redMaPPer catalogue (Rykoff et al. 2014);  $\lambda$  is the redMaPPer richness defined as the sum of the membership probabilities over all galaxies; offset relatives to the maxBCG center. <sup>c</sup>: From the second Planck catalogue of SZ sources (Planck Collaboration et al. 2016); the significance of the Planck detection and the offset to maxBCG center.

covering nearly 10000 deg<sup>2</sup> of sky. Each cluster is identified as an overdensity of red-sequence galaxies, which relies on iteratively self-training a model of the red-sequence as a function of redshift based on the red galaxies with known spectroscopic redshifts. Then this model is used on photometric data to assign membership probabilities to galaxies with luminosities  $\geq 0.2L_*$  in the cluster vicinity. The cluster richness  $\lambda$  is the sum of the membership probabilities of the galaxies within a radius  $R_\lambda$ , which scales with richness as  $R_\lambda = (\lambda/100)^{0.2} h^{-1}$  Mpc. The cluster photometric redshift is evaluated by simultaneously fitting all high probability

cluster members with a single red sequence model, with an accurate of 0.005-0.01. The cluster center is on the central galaxy chosen with a probabilistic approach that weights not just galaxy luminosity, but also local galaxy density, as well as the consistency to cluster redshift. The completeness is  $\gtrsim 99\%$  at  $\lambda > 30$  and  $z < 0.3$ , and the purity is  $> 95\%$  at all richness and redshift. The redMaPPer cluster mass has been calibrated by Simet et al. (2017) with the  $M_{200m} - \lambda$  relation. We convert  $M_{200m}$  to  $M_{500c}$  assuming a cluster mass distribution of Navarro-Frenk-White (NFW; Navarro et al. 1997) profile with a typical concentration of 6 (e.g., Buote

et al. 2007) and a median  $z = 0.23$  for the sample. The ratio  $M_{200m}/M_{500c}$  is 1.67.

### 2.3 PSZ2 catalogue

The second *Planck* Catalogue of Sunyaev-Zel'dovich Sources (PSZ2; [Planck Collaboration et al. 2016](#)) exploits the 29 month full-mission data. It contains 1653 candidate clusters with a signal-to-noise ratio (SNR) above 4.5 and distributes across 83.6% of the sky. Among them, more than 1203 are confirmed to be clusters with identified counterparts in external optical or X-ray samples or by dedicated follow-ups, and with a purity larger than 83%. The median redshift is  $z \sim 0.2$  and the farthest clusters are at  $z \lesssim 1.0$ .

## 3 DATA ANALYSIS

Table 2 provides the detail of observations from *Chandra* and *XMM-Newton* for this sample. We present here the data reduction procedure, the derivation of X-ray properties, and how we deal with complicated multiple cluster systems.

### 3.1 Chandra

We process the *Chandra* ACIS data with the *Chandra* Interactive Analysis of Observation (CIAO, version 4.9) and calibration database (CALDB, version 4.7.5.1), following the procedures in [Morandi et al. \(2015\)](#). We reprocess the level-1 event files using `acis_process_events` tool to check for the presence of cosmic ray background events, correct for spatial gain variations due to charge transfer inefficiency (CTI), and recompute the event grades. We then filter the data to include the standard events grades 0, 2, 3, 4, and 6 only. Most observations were taken in very faint (VFAINT) mode, and in this case we applied VFAINT cleaning to both the cluster and stowed background observations. The light curve is then created with `dmextract` and filtered with `deflare` to exclude intervals of deviating more than  $3\sigma$  of the mean value. Then we filter the ACIS event files in 0.3–12 keV to obtain a level-2 event file. Point sources and extended substructures are detected and removed using `wavedetect`, which provides candidate point sources, and the result is then checked through visual inspection. We produce the X-ray images from the level-2 event file and then create an exposure-corrected image from a set of observations using `merge_obs` (Fig. C1). We then measure the surface brightness radial profile  $S_X$  from the exposure-corrected images. We applied a direct subtraction of the cosmic X-ray (CXB)+particle+readout artifact backgrounds. For the particle background modeling, we use the stowed background scaled with the count rate in the 9.5–12 keV band, where the *Chandra* effective area is negligible and the flux is dominated by the particle background. In order to measure the CXB, we considered the region where the CXB is more dominant than the cluster emission, which can be determined from the flattened portion at the outer radial profile.

The spectra and response files of ACIS (0.7–7 keV) are extracted using `specextract` and fitted with `XSPEC` package ([Arnaud 1996](#), version 12.9.1). We adopt the APEC emissivity model ([Foster et al. 2012](#)) to fit the on-cluster emission and

the AtomDB (version 3.0.8) database of atomic data, the solar abundance tables are adopted from [Asplund et al. \(2009\)](#) and fixed to  $0.3 Z_\odot$ , the redshift is fixed to the optical spectroscopy redshift of BCG. We apply the Tuebingen-Boulder absorption model (TBABS) for X-ray absorption by the interstellar medium (ISM), with fixed hydrogen column density  $N_H$  to the Galactic value from the `NHtot` tool ([Willingale et al. 2013](#)). The off-cluster background spectra are extracted from cluster emission insignificant regions ( $\gtrsim R_{100}$ ) of the same exposure.

### 3.2 XMM-Newton

We reduce the *XMM-Newton* MOS and pn data using the Extended Source Analysis Software (ESAS; [Kuntz & Snowden 2008](#); [Snowden et al. 2008](#)), as integrated into the *XMM-Newton* Science Analysis System (version 15.0.0) with the associated Current Calibration Files (CCF), following the procedures in [Ge et al. \(2016\)](#). We reproduce the raw event files from MOS and pn CCDs using tasks `emchain` and `epchain`, respectively. The solar soft proton flares are filtered out with `mos-filter` and `pn-filter` through the light curve screening to obtain the clean event files. The MOS CCDs that are damaged or in the anomalous state are excluded in downstream processing. The point sources are detected by `cheese` and checked with visual inspection and then excluded. We use `mos-spectra` and `pn-spectra` to produce event images and exposure maps, as well as to extract spectra and response files. The instrumental background images and spectra are modeled with `mos_back` and `pn_back`. We combine the event images, background images, and exposure maps from MOS and pn with `comb`, and combine the images from multiple observations with `merge_comp_xmm`. We use `adapt` to produce the final background subtracted, exposure corrected, and smoothed images (Fig. C1). The surface brightness profiles are extracted from exposure corrected images of combined MOS1/MOS2 and pn separately. The derived X-ray properties are evaluated with error weight means of MOS and pn.

The spectra of MOS (0.3–11.0 keV) and pn (0.4–11.0 keV) are fitted jointly. The on-cluster spectra are also fitted with APEC model. The same solar abundance table, AtomDB version and the Galactic absorption model as in the *Chandra* analysis are used. The background spectra consist of mainly four components: CXB, quiescent particle background (QPB), residual soft proton (SP), and solar wind charge exchange (SWCX). They are fit simultaneously with the on-cluster emission. The CXB is modeled with three components: an unabsorbed thermal emission ( $E \sim 0.1$  keV) from the local hot bubble or heliosphere; an absorbed thermal emission ( $E \sim 0.25$  keV) from the Galactic halo and/or intergalactic medium; and an absorbed power-law emission ( $\Gamma \sim 1.46$ ) from an unresolved background of cosmological sources. An off-cluster ROSAT all-sky survey (RASS) spectrum is also extracted from a  $1^\circ - 2^\circ$  annulus surrounding the cluster and joint fit with other spectra to constrain the contribution of CXB. The QPB originates from the interaction of cosmic rays with detectors. The QPB continuum is subtracted as background spectra in `XSPEC`, while its bright instrumental fluorescent lines vary from observation to observation. Thus, they are not included in the QPB model spectra and are individually fit by Gaussian models. The



**Table 2.** X-ray observations of the richest maxBCG clusters

Cluster	$N_{\mathrm{H}}$ $10^{20}\mathrm{cm}^{-2}$	<i>Chandra</i> id	<i>Chandra</i> time ks	<i>XMM-Newton</i> id	<i>XMM-Newton</i> time ks
A2142	4.36	(1196 1228 5005 7692) (15186 16564 16565)	(231.2)	(0111870101 0111870401) 0674560201	51.5, 52.9, 41.1/108.7
J150	2.59	-	-	0742510101* 0761590101*	7.9, 7.8, 5.7/43.6
A1689	1.98	540 1663 5004 6930 7289 7701	196.7/199.8	0093030101	34.4, 35.3, 26.3/39.8
A1443	2.41	11762 16279	25.5/26.1	-	-
A781	1.75	(534 15128)	(45.6)	0150620201 0401170101 0401170201	73.1, 74.8, 58.2/105.2
A1986	3.18	17474	5.0/5.1	-	-
A1882	3.76	12904 12905 12906 12907 12908 12909 12910 12911 12912 17149 17150 17151 17671	392.2/397.9	0145480101 0762870501	30.2, 30.9, 20.0/45.6
A1758	1.06	(2213) 7710 13997 15538 15540	154.7/215.8	(0142860201)	(57.2)
A1760	1.87	17159	7.0/7.1	-	-
A1622	1.19	11763 (17154)	12.9/27.1	-	-
A750	3.66	924 7699	34.5/34.9	0605000901 0673850901	21.0, 21.2, 9.7/45.7
A1682	1.07	3244 11725	29.4/30.0	-	-
A1246	1.66	11770	5.0/5.1	-	-
A1961	1.21	11764	6.9/7.0	-	-
A2034	1.62	(2204 7695 12885 12886 13192 13193)	(259.1)	0149880101 0303930101 0303930201	18.8, 19.5, 11.1/75.4
A655	4.39	15159	7.9/8.1	-	-
A1914	1.10	(542) 3593 12197 12892 12893 12894	38.6/47.2	0112230201	19.1, 20.3, 8.8/25.8
Z5247	1.73	539 11727	29.3/30.5	(0673851101 0673852101)	(46.1)
A657	3.38	-	-	0742510401*	14.9, 15.7, 8.4/18.0
J229	6.09	-	-	0201902001 0201902101 0761590301*	76.0, 76.6, 58.4/83.8
A1423	1.93	538 11724	35.5/36.0	-	-
A801	4.37	11767	6.6/6.7	-	-
A773	1.34	533 3588 5006 13592 13594 13593 13591	60.2/ 61.3	0084230601	12.5, 14.3, 14.2/25.2
A1576	1.12	7938 15127	43.4/45.0	(0402250101 0402250601)	(28.8)
A2631	3.96	3248 11728	26.0/26.3	(0042341301)	(14.0)
A1703	1.39	15123 (16126)	29.1/78.8	(0653530101 0653530201 0653530301) (0653530401 0653530501 0653530601) (0653530701 0653530801 0653530901)	(135.5)
A2219	1.87	(896) 7892 13988 14431 14451 14355 14356	152.5/197.4	(0112231801 0112231901) 0605000501	12.0, 12.8, 6.8/55.1
A1319	2.20	11760 17153	23.8/24.1	-	-
A1560	2.63	11761 (17155)	12.1/20.8	(0404120101)	(31.9)
J175	4.51	-	-	0655380101	4.2, 4.3, 3.1/13.9
J249	1.94	-	-	0761590401*	20.2, 20.7, 13.7/23.0
A1201	1.66	(4216 7697) 9616	47.4/93.2	(0500760101)	(51.8)
A2009	3.89	10438	19.9/20.1	(0673851001 0673852201) 0693011001 (0693011301)	10.6, 12.3, 6.1/ 60.2
A2111	2.00	544 11726	31.2/31.6	(0673850601 0673852301)	(40.5)
A815	1.98	-	-	0742510701*	16.1, 16.6, 12.5/20.0
Z1450	1.19	-	-	0761590601*	19.6, 19.9, 6.3/23.0
A1765	2.33	-	-	0761590701*	21.7, 21.4, 15.6/ 24.0
A1902	1.02	16151	5.0/5.1	-	-

*Note.* The total Galactic column density of Hydrogen is from [Willingale et al. \(2013\)](#). The obsids and their total exposure time in brackets are not included in the data analysis of this work. The exposure time is the clean/total time for *Chandra* or clean MOS1, MOS2, pn/total time for *XMM-Newton*. The obsids with \* are clusters from our *XMM* project (proposal id 74251 and 76159, PI: Sun).

residual SP may still exist after the light-curve screening. As they are not X-ray photons and not folded through the instrumental effective area, SP is modeled by a power law with diagonal response matrices supplied with the ESAS calibration files. The SWCX process may produce additional emission lines in the observed spectra, and they are modeled with the Gaussian components.

Table 3. X-ray properties

Cluster	RA	DEC	$z_{\text{spec}}$	$T_X$ keV	$L_X$ $10^{44} \text{ erg s}^{-1}$	$Y_X$ $10^{14} M_\odot \text{ keV}$	$R_{500}$ Mpc	offset <sup>N</sup> kpc	offset <sup>λ</sup> kpc	$M_{500}$ $10^{14} M_\odot$	$M_{500}^N$ $10^{14} M_\odot$	$M_{500}^{\lambda}$ $10^{14} M_\odot$	opt <sup>N</sup>	opt <sup>λ</sup>
A2142	239.58563	27.22967	0.091	$8.20 \pm 0.05$ (X)	$32.24 \pm 0.06$	$11.44 \pm 0.33$	1.43	25.7	25.8	9.1	13.5	12.9	R	R
J150M	150.61145	20.51861	0.320	$3.63 \pm 0.48$ (X)	$3.24 \pm 0.12$	$0.98 \pm 0.15$	0.81	1273.2	888.0	2.1	11.7	11.1	M, P	M, P
J150E	150.68539	20.49089	0.309	$2.44 \pm 0.35$ (X)	$1.08 \pm 0.05$	$0.28 \pm 0.05$	0.65			1.1				
J150W	150.55545	20.53728	0.320	$3.11 \pm 0.71$ (X)	$1.00 \pm 0.09$	$0.55 \pm 0.14$	0.74			1.6				
A1689	197.87247	-1.34129	0.183	$10.27 \pm 0.26$ (C)	$38.32 \pm 2.03$	$13.94 \pm 0.42$	1.54	5.4	5.8	12.5	11.1	12.4	R	R
A1443	180.30410	23.10630	0.264	$8.01 \pm 0.13$ (X)	$33.59 \pm 0.11$	$8.86 \pm 0.37$	1.34			8.3				
A781	140.11223	30.49477	0.299	$8.56 \pm 1.35$ (C)	$17.09 \pm 0.95$	$8.16 \pm 1.73$	1.34	216.3	112.2	8.9	9.8	9.2	M	M
A781M	140.22101	30.46535	0.293	$5.55 \pm 0.17$ (X)	$10.03 \pm 0.08$	$3.88 \pm 0.22$	1.03	67.3	179.0	4.3	8.9	1.2	M, P	M, P
A781E	140.29418	30.46433	0.429	$3.12 \pm 0.14$ (X)	$0.75 \pm 0.06$	$2.32 \pm 0.15$	0.75		71.7	1.7		8.9	M, P	M, P
A781W	139.89517	30.53303	0.427	$3.34 \pm 0.34$ (X)	$3.26 \pm 0.09$	$0.83 \pm 0.10$	0.72		84.5	1.7		1.8	M, P	M, P
A1986	223.28780	21.89560	0.117	$3.24 \pm 0.24$ (X)	$2.81 \pm 0.06$	$0.62 \pm 0.06$	0.71			1.6				
A1882E	213.78363	-0.49265	0.139	$4.41 \pm 0.66$ (C)	$1.84 \pm 0.11$	$1.26 \pm 0.31$	1.00	639.5	23.5	3.2	8.4	3.9	M	R
A1882W	213.60034	-0.37877	0.138	$2.37 \pm 0.17$ (X)	$0.62 \pm 0.04$	$0.24 \pm 0.02$	0.70	13.0		1.1	8.0		P	
A1882M	213.74050	-0.34915	0.139	$2.22 \pm 0.17$ (X)	$0.55 \pm 0.02$	$0.22 \pm 0.02$	0.68		10.0	1.0		6.8	P	
A1882N	213.53597	-0.27103	0.140	$1.91 \pm 0.16$ (X)	$0.33 \pm 0.01$	$0.14 \pm 0.02$	0.63			0.8				
A1758N	203.19958	50.53972	0.279	$1.37 \pm 0.08$ (X)	$0.27 \pm 0.01$	$0.06 \pm 0.01$	0.52			0.5				
A1758S	203.12317	50.40931	0.273	$1.36 \pm 0.14$ (X)	$0.11 \pm 0.01$	$0.04 \pm 0.01$	0.52			0.5				
A1760	203.53550	20.23500	0.173	$8.64 \pm 0.57$ (C)	$18.18 \pm 2.46$	$8.63 \pm 1.77$	1.33	491.0	492.0	8.9	8.0	11.2	M, P	M, P
A1622	192.42163	49.87525	0.283	$6.59 \pm 0.18$ (C)	$13.18 \pm 1.71$		1.15		203.7	5.7		2.7	M, P	M, P
A750E	137.30282	10.97472	0.176	$7.93 \pm 1.07$ (C)	$5.68 \pm 0.27$	$4.46 \pm 0.92$	1.34	138.4	1001.5	8.2	7.9	4.2	M	M
A750W	137.21662	11.02747	0.164	$4.76 \pm 0.87$ (C)	$2.09 \pm 0.10$	$1.51 \pm 0.52$	0.96	477.3	604.1	3.3	7.4	9.0	M, P	M, P
A1682	196.70864	46.55945	0.218	$5.57 \pm 0.44$ (C)	$6.07 \pm 0.87$	$2.61 \pm 0.55$	1.11		23.7	4.6		13.4	P	
A1246	170.98878	21.48200	0.193	$4.76 \pm 0.16$ (X)	$5.83 \pm 0.06$	$2.04 \pm 0.12$	1.02			3.6				
A1961	221.13280	31.22670	0.233	$3.36 \pm 0.18$ (X)	$1.96 \pm 0.04$	$0.86 \pm 0.07$	0.84	13.0		2.0	7.4	8.3	P	R
A2034	227.55129	33.50973	0.112	$5.95 \pm 0.71$ (C)	$11.24 \pm 0.82$	$4.05 \pm 0.59$	1.12	159.7	3.6	5.0	7.4	8.3	M	R
A655	126.37410	47.13130	0.129	$6.03 \pm 0.99$ (C)	$10.25 \pm 0.51$	$3.49 \pm 0.59$	1.15	312.3	68.4	5.2	7.1	7.6	M	M
A1914	216.50380	37.82557	0.170	$3.03 \pm 0.46$ (C)	$2.71 \pm 0.20$	$0.62 \pm 0.14$	0.77	1005.8	3.8	1.6	7.0	7.7	M	R
Z5247	188.57520	9.77170	0.231	$5.98 \pm 0.17$ (X)	$8.82 \pm 0.06$	$3.96 \pm 0.20$	1.19	174.0	174.0	5.3	6.9	6.4	M	M
A657	125.83066	15.96316	0.153	$3.97 \pm 0.31$ (C)	$3.37 \pm 0.09$	$1.08 \pm 0.12$	0.94	25.0	25.4	2.7	6.9	9.2	R	R
J229	229.33991	-0.71679	0.114	$9.18 \pm 0.91$ (C)	$32.74 \pm 1.64$	$10.33 \pm 1.20$	1.46	174.9	174.9	10.5	6.8	6.7	M	M
A2051	229.18317	-0.97167	0.120	$7.84 \pm 0.19$ (X)	$29.39 \pm 0.14$	$8.71 \pm 0.39$	1.34			8.1				
A2051S	229.24147	-1.11056	0.117	$6.03 \pm 1.23$ (C)	$7.52 \pm 0.74$	$5.58 \pm 1.79$	1.12	79.1	35.3	5.1	6.8	5.8	M, P	P
A2051N	229.10108	-0.83036	0.376	$2.89 \pm 0.17$ (X)	$1.28 \pm 0.02$	$0.53 \pm 0.05$	0.78	5.2	5.2	1.6	6.5	4.9	R	R
				$2.50 \pm 0.12$ (X)	$0.61 \pm 0.01$	$0.29 \pm 0.03$	0.73	178.3	12.5	1.3	6.4	3.1	M, P	P
				$3.78 \pm 0.13$ (X)	$2.28 \pm 0.03$	$1.18 \pm 0.08$	0.92			2.5				
				$2.45 \pm 0.26$ (X)	$0.27 \pm 0.01$	$0.15 \pm 0.02$	0.73	4.6	233.6	1.2	1.3	2.8	R	M
				$3.43 \pm 0.52$ (X)	$1.70 \pm 0.13$	$0.68 \pm 0.14$	0.76	6.2		1.8		1.1		R

Table 3 (cont'd)

Cluster	RA	DEC	$z_{\text{spec}}$	$T_X$ keV	$L_X$ $10^{44} \text{ erg s}^{-1}$	$Y_X$ $10^{14} M_\odot \text{ keV}$	$R_{500}$ Mpc	offset <sup>N</sup> kpc	offset <sup><math>\lambda</math></sup> kpc	$M_{500}$ $10^{14} M_\odot$	$M_{500}^N$ $10^{14} M_\odot$	$M_{500}^\lambda$ $10^{14} M_\odot$	opt <sup>N</sup>	opt <sup><math>\lambda</math></sup>
A2050	229.07404	0.08937	0.121	$4.46 \pm 0.12$ (X)	$4.05 \pm 0.04$	$1.69 \pm 0.10$	1.01	5.9	5.8	3.3	4.9	4.6	R	R
A1423	179.32222	33.61106	0.214	$6.61 \pm 0.53$ (C)	$13.62 \pm 0.68$	$4.89 \pm 0.52$	1.19	1.6	93.5	6.0	6.3	5.2	R	M
A801	142.01930	20.53110	0.192	$6.26 \pm 0.73$ (C)	$5.16 \pm 0.24$	$2.65 \pm 0.46$	1.17	22.2	22.3	5.5	6.3	5.8	R	R
A773	139.47280	51.72909	0.217	$7.53 \pm 0.49$ (C)	$16.87 \pm 0.74$	$7.09 \pm 0.30$	1.28	26.0	25.3	7.4	6.2	11.3	R	R
				$6.53 \pm 0.17$ (X)	$14.68 \pm 0.11$	$5.31 \pm 0.27$	1.18			5.8				
A1576	189.24296	63.18712	0.301	$7.14 \pm 0.83$ (C)	$12.34 \pm 1.85$	$6.11 \pm 0.59$	1.18	29.4	9.2	6.5	6.1	6.6	R	R
A2631	354.41084	0.26799	0.277	$7.15 \pm 0.82$ (C)	$15.85 \pm 0.79$	$6.76 \pm 1.73$	1.20	87.9	87.8	6.6	6.0	8.7	M	M
A1703	198.77059	51.81964	0.282	$5.95 \pm 0.33$ (C)	$19.89 \pm 0.99$	$4.27 \pm 1.74$	1.08	36.9	35.8	4.8	6.0	11.2	R	R
A2219	250.08197	46.71113	0.225	$10.81 \pm 0.31$ (C)	$65.86 \pm 3.29$	$18.38 \pm 3.18$	1.55	6.7	7.3	13.3	5.8	16.0	R	R
A1319M	174.05510	40.04070	0.290	$3.75 \pm 0.60$ (C)	$1.58 \pm 0.29$	$0.64 \pm 0.15$	0.84	41.2	41.2	2.2	5.8	11.4	P	P
A1319NW	173.99769	40.08607	0.295	$4.62 \pm 1.77$ (C)	$1.41 \pm 0.42$		0.93			3.2				
A1560	188.47084	15.19453	0.284	$5.31 \pm 0.71$ (C)	$4.33 \pm 0.33$	$2.24 \pm 0.42$	1.02	1.8	308.8	4.0	5.8	9.7	P	M, P
J175N	175.56923	10.45006	0.117	$1.66 \pm 0.32$ (X)	$0.20 \pm 0.01$		0.59	1205.2	47.3	0.6	5.8	0.9	M, P	P
J175S	175.52926	10.14652	0.119	$1.42 \pm 0.40$ (X)	$0.14 \pm 0.02$		0.54		24.8	0.5	-	1.8	P	P
J249SW	249.90682	47.05049	0.227	$3.51 \pm 0.28$ (X)	$1.76 \pm 0.04$	$0.71 \pm 0.07$	0.83	338.3	33.9	2.1	5.8	3.4	M, P	P
J249NE	250.03190	47.16119	0.224	$2.67 \pm 0.64$ (X)	$0.77 \pm 0.03$	$0.30 \pm 0.08$	0.72			1.3	-	-		
A1201	168.22715	13.43506	0.168	$6.47 \pm 0.41$ (C)	$9.34 \pm 0.47$	$4.02 \pm 0.79$	1.21	8.1	452.8	5.9	5.7	4.6	R	M
A2009	225.08160	21.36920	0.153	$6.82 \pm 0.20$ (C)	$17.54 \pm 0.21$	$5.10 \pm 0.20$	1.25	3.2	3.3	6.5	5.6	5.7	R	R
				$5.91 \pm 0.21$ (X)	$14.04 \pm 0.10$	$3.96 \pm 0.24$	1.16			5.1				
A2111	234.92407	34.41675	0.228	$8.66 \pm 0.75$ (C)	$14.07 \pm 0.80$	$8.21 \pm 1.62$	1.37	114.4	114.4	9.2	5.5	11.1	M	M
A815	143.03589	29.06782	0.300	$2.58 \pm 0.30$ (X)	$1.47 \pm 0.05$		0.68	0.2	0.0	1.2	5.5	5.7	P	P
Z1450	223.05214	37.88133	0.282	$2.30 \pm 0.40$ (X)	$1.48 \pm 0.05$	$0.34 \pm 0.07$	0.64	60.2	28.6	1.0	5.4	6.5	M, P	P
A1765	204.20616	10.44110	0.155	$2.22 \pm 0.16$ (X)	$0.49 \pm 0.02$	$0.20 \pm 0.02$	0.67	11.1	11.1	1.0	5.3	5.0	P	P
A1902	215.41900	37.29160	0.163	$6.64 \pm 0.52$ (C)	$10.53 \pm 0.26$	$3.51 \pm 0.49$	1.23	16.3	16.3	6.2	5.3	4.9	R	R

Note. The individual cluster name is marked the same as in Fig. C1. RA and DEC are the X-ray peak position.  $z_{\text{spec}}$  is the spectroscopic redshift of BCG.  $T_X$  is the X-ray temperature within  $0.15\text{--}0.75 R_{500}$ .  $L_X$  is the bolometric luminosity within  $R_{500}$ .  $Y_X$  is not listed if the extrapolation factor for  $M_{\text{gas}}$  is larger than 1.5.  $R_{500}$  and  $M_{500}$  are estimated from the  $M - T_X$  relation from (Sum et al. 2009). offset<sup>N</sup> or offset <sup>$\lambda$</sup>  is the offset between X-ray peak and maxBCG or redMaPPer center, respectively.  $M_{500}^N$  and  $M_{500}^\lambda$  is from  $M - N$  relation (Rozo et al. 2009) for maxBCG and  $M - \lambda$  relation (Simet et al. 2017) for redMaPPer, respectively. We note that there are  $\sim 10\%$  and  $\sim 3\%$  correction for the maxBCG and redMaPPer masses because we cite  $\bar{a}_{m/n}$  from  $M - N$  relation and  $\bar{a}_{m/n} = a_{m/n} + \frac{1}{2} \sigma_{m/n}^2$  (Appendix A). The label of “M” means clusters with Miscentering problems (the offset between X-ray peak and optical center larger than 50 kpc). “P” means clusters with Projection problems (another X-ray cluster in a 2 Mpc radius) and “R” means Relaxed cluster without both miscentering and projection problems.

### 3.3 $T_X$ , $L_X$ , and $Y_X$

The spectroscopic X-ray temperature  $T_X$  is measured in  $0.15 - 0.75 R_{500}$ . The inner boundary of  $0.15 R_{500}$  is chosen to exclude the central cool core and the outer boundary of  $0.75 R_{500}$  is limited by the quality of the spectroscopic data. The X-ray peak or centroid of a cluster is the position where the derivatives of the surface brightness variation along two orthogonal (e.g. X and Y) directions become zero.  $R_{500}$  is estimated from the  $M - T_X$  relation (Sun et al. 2009) iteratively. In fact, the  $R_{500}$  is weakly dependent on temperature with a power-law index of 0.55 and the  $R_{500}$  typically converges in three iterations.

The bolometric X-ray luminosity  $L_X$  is derived within  $R_{500}$ . We sum the count rates from surface brightness profiles in the 0.7-2 keV for *Chandra* (maximize the SNR of cluster emission and minimize the dependency of the cooling function on the temperature and metallicity) and 0.7-1.3 keV for *XMM-Newton* (maximize the SNR of cluster emission and minimize the contamination of SWCX lines below 0.7 keV and instrumental lines above 1.3 keV). Regions masked for point sources, chip gaps and bad pixels are added back in this process. We then use the best-fit spectral model to convert the count rate to bolometric luminosity. For some clusters with shallow data, surface brightness profiles can not be robustly constrained to  $R_{500}$ . We extrapolate the surface brightness profile using a power law measured from the profile at large radii. The typical slope is about -3, which corresponds to  $\beta = 2/3$  for a  $\beta$  model and is typical for cluster density profiles around  $R_{500}$  (Morandi et al. 2015). The extrapolated correction factors ( $[\text{data} + \text{extrapolation}] / \text{data}$ ) are always smaller than 1.5.

The X-ray Compton parameter  $Y_X$ ,  $M_{\text{gas}} (< R_{500}) \times T_X$  ( $0.15 - 1.0 R_{500}$ ), is also derived. We convert our  $T_X$  ( $0.15 - 0.75 R_{500}$ ) to  $T_X$  ( $0.15 - 1.0 R_{500}$ ) with the correction factor of 0.96 based on Morandi et al. (2015). The gas mass  $M_{\text{gas}}$  within  $R_{500}$  is summed from the gas density profile, which is derived from deprojecting the surface brightness profile. For clusters with surface brightness profiles not reaching  $R_{500}$ , we also extrapolate the gas density profiles using a power-law model measured from the profile at large radii, similar to what we did for luminosity extrapolation. The resulting  $Y_X$  value is only included in the analysis if the extrapolated correction factor of  $M_{\text{gas}}$  ( $[\text{data} + \text{extrapolation}] / \text{data}$ ) is smaller than 1.5. Table 3 includes the results of X-ray properties.

### 3.4 Multiple cluster systems

Most clusters in the sample are mergers. Some clusters with multiple components, e.g., J150, A781, A750 and A1319, require special attention as the association of the X-ray emission with the optical cluster becomes ambiguous. We apply different strategies to deal with such systems.

For systems of one optical cluster corresponding to multiple X-ray clusters (e.g., J150, A750, A1319), we use two different methods to associate the X-ray emission with the optical cluster and study the scaling relations.

i) Add. The X-ray properties are derived individually for each cluster after masking the  $R_{500}$  region of the nearby cluster. Then we add their properties ( $L_X$  and  $Y_X$ ) together and assign to the corresponding optical counterpart from maxBCG or redMaPPer catalogue. For instance, A750 is a

close pair composed of A750E and A750W (Fig. C1, Appendix C). Both maxBCG and redMaPPer catalogue mix them as one cluster. We add the  $L_X$  values from A750E and A750W, as well as their  $Y_X$  values. We do not add the  $T_X$ .

ii) Mix. The multiple subclusters are treated as one cluster. We center the cluster on the peak of the X-ray brightest subcluster and derived the X-ray properties within  $R_{500}$  determined from the  $M - N$  relation based on the optical catalogue, under the assumption of spherical symmetry. In the case of A750, we center the cluster in A750E and do not mask out A750W.

We compare the results in Table 4 from these two methods and find that the  $L_X$  are comparable from add and mix, while the  $Y_X$  from add is smaller than the  $Y_X$  from mix. For clusters in the early merge stage (J150, A750, A1319 and J175), we use the add method. For clusters in the late merge stage (Z5247, A1560 and A815) where the individual  $R_{500}$  regions heavily overlap, we use the mix method. We emphasize that switching the method for multiple cluster systems in Table 4 does not affect any of our conclusions for the whole sample.

For systems of one X-ray cluster corresponding to multiple optical clusters (e.g., A781, A1760, A2631), we match the X-ray cluster with the richest optical cluster.

## 4 RESULTS

We first study the scaling relations between X-ray and optical properties as  $T_X - N$ ,  $L_X - N$ , and  $Y_X - N$  relations. We then study the X-ray scaling relations as  $L_X - T_X$  and  $L_X - Y_X$  relations. Finally we classify the clusters using quantitative X-ray morphology parameters.

### 4.1 X-ray — optical scaling relations

Fig. 1 left panel shows the  $T_X - N_{200}$  relation for this sample, along with the expected relation from the X-ray  $M - T_X$  relation and the weak-lensing  $M - N_{200}$  relation using the multivariate scaling relation in Appendix A. Four clusters with multiple subclusters (see Section 3.4) are not included in the temperature - richness plot but they are included in the luminosity - richness plot. While the richness threshold of 78 corresponds to  $\sim 5$  keV, a wide temperature range of from  $\sim 2$  keV to  $\sim 10$  keV is observed from the data, with approximately half of the systems cooler than 5 keV (the median temperature for the nine subclusters in the four clusters left out is  $\sim 3.4$  keV). The temperature distribution is not symmetric around the expected relation, but with more outliers towards lower temperatures. Indeed, 29 clusters in the sample are detected in the PSZ2 catalogue and the maxBCG clusters without *Planck* detections all have low temperatures (Fig. 1). This contamination of low-temperature systems may help to explain part of the mismatch between the SZ stacking and the expectation based on the optical richness. Fig. 1 right panel shows the  $T_X - \lambda$  relation of the sample, with the same X-ray  $M - T_X$  relation and various  $M - \lambda$  relations. The cluster mass comes from weak lensing (Simet et al. 2017), galaxy velocity dispersion (Farahi et al. 2016), and CMB weak-lensing (Baxter et al. 2018). Although the scatter of redMaPPer is smaller than that of maxBCG, there



**Table 4.** Assignment table for multiple cluster system

Cluster	Subclusters	maxBCG $T_X, L_X, Y_X$	redMaPPer $T_X, L_X, Y_X$
J150	J150E, J150M, J150W (add)	-, $5.32 \pm 0.16$ , $1.81 \pm 0.21$	-, $5.32 \pm 0.16$ , $1.81 \pm 0.21$
	J150E, J150M, J150W (mix)	$2.89 \pm 0.28$ , $5.54 \pm 0.15$ , $2.95 \pm 0.35$	$2.94 \pm 0.29$ , $5.47 \pm 0.14$ , $2.88 \pm 0.35$
A750	A750E, A750W (add)	-, $7.79 \pm 0.07$ , $2.90 \pm 0.68$	-, $7.79 \pm 0.07$ , $2.90 \pm 0.68$
	A750E, A750W (mix)	$4.01 \pm 0.11$ , $7.16 \pm 0.07$ , $3.88 \pm 0.21$	$3.66 \pm 0.12$ , $7.35 \pm 0.07$ , $4.09 \pm 0.24$
Z5247	Z5247NE, Z5247SW (mix)	$6.03 \pm 1.23$ , $7.52 \pm 0.74$ , $5.58 \pm 1.79$	$6.03 \pm 1.23$ , $7.52 \pm 0.74$ , $5.58 \pm 1.79$
A1319	A1319M, A1319NW, A1319SW (add)	-, $2.99 \pm 0.51$ , -	-, $2.99 \pm 0.51$ , -
A1560	A1560NW, A1560SE (mix)	$5.31 \pm 0.71$ , $4.33 \pm 0.33$ , $2.24 \pm 0.42$	$5.31 \pm 0.71$ , $4.33 \pm 0.33$ , $2.24 \pm 0.42$
J175	J175N, J175S (add)	-, $0.34 \pm 0.02$ , -	-
A815	A815N, A815S (mix)	$2.63 \pm 0.30$ , $1.57 \pm 0.06$ , -	$2.58 \pm 0.30$ , $1.47 \pm 0.05$ , -

*Note.* For systems of one optical cluster corresponding to multiple X-ray clusters, we use two different methods to assign the X-ray properties for clusters in different merge stages. The add method adds  $L_X$  or  $Y_X$  of multiple clusters. The mix method treats the multiple clusters as one cluster and uses the same routines for the single cluster, then derives the X-ray properties centering on the brightest X-ray peak within  $R_{500}$  from  $M-N$  relations.

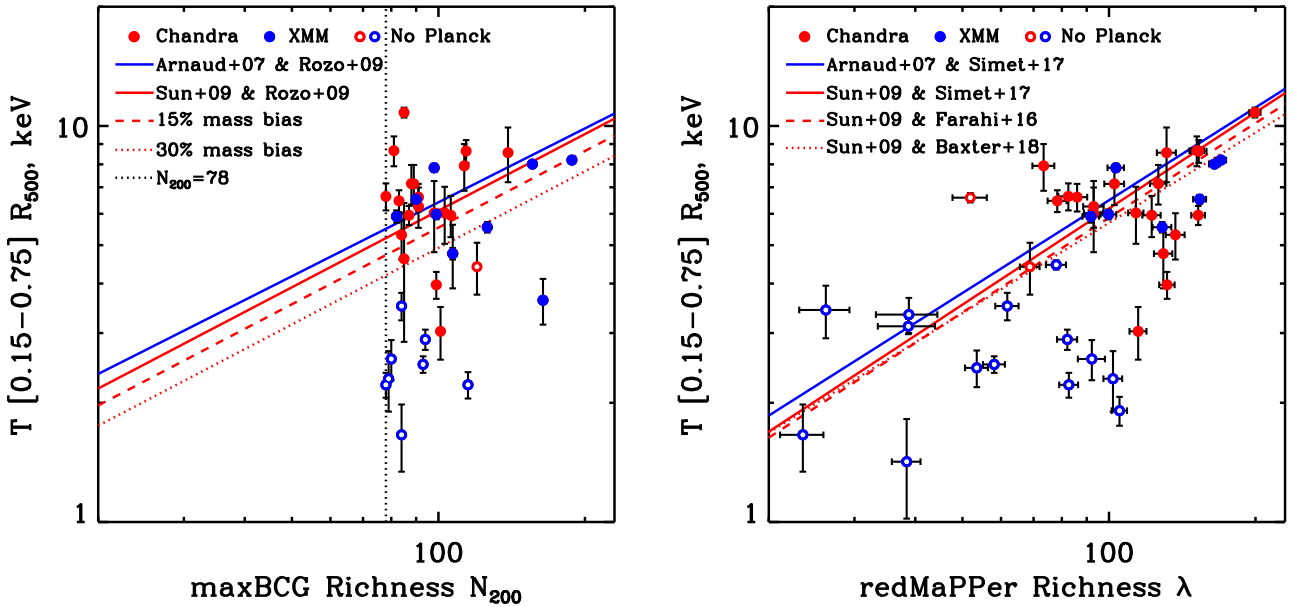


**Figure 1.** Left: the  $T_X - N_{200}$  relation for the richest maxBCG sample, with  $T_X$  measured from *Chandra* (red) or *XMM-Newton* (blue). The empty circles are clusters without *Planck* SZ detection. The solid lines are the expected  $T_X - N_{200}$  relations from  $M - T_X$  relation (blue for *XMM-Newton* calibration, Arnaud et al. 2007; red for *Chandra*, Sun et al. 2009) and weak-lensing  $M - N_{200}$  relation (Rozo et al. 2009) on the full maxBCG sample (see Appendix A for the detail and bias correction). The dashed line shows 15% hydrostatic bias (the X-ray mass is 15% lower than the weak lensing mass), and dotted line shows 30% hydrostatic bias (approximately equivalent to 21% hydrostatic bias with 10% weak-lensing bias, which induces 10% overestimate of true cluster mass, as discussed in Rozo et al. 2014b). The black dotted line marks the richness threshold of  $N_{200} = 78$ . Right: the  $T_X - \lambda$  relation for the same sample. The X-ray  $M - T_X$  relations are combined with the  $M - \lambda$  relation from weak-lensing (Simet et al. 2017; solid line), galaxy velocity dispersion (Farahi et al. 2016; dashed line), and CMB weak-lensing (Baxter et al. 2018; dotted line). Four clusters (J150, A750, A1319 and J175) with multiple subclusters are not included in these two figures but they are included in Figs. 2-3. There are more redMaPPer clusters than maxBCG clusters because redMaPPer catalogue identifies more clusters in some multi cluster systems in Table 3. There are more *XMM* outliers than *Chandra*, which reflects the fact that many *XMM* clusters were selected for observations with non-X-ray reasons, including seven clusters in our new *XMM* project. Moreover, most of these low  $T_X$  outliers have no *Planck* SZ detection.

are still more outliers towards lower temperatures compared with the model prediction.

Fig. 2 shows the  $L_X - N$  relation for maxBCG (left panel) and redMaPPer (right panel). The solid line shows the expected  $L_X - N$  relation combined from the  $L_X - M$  relation and the  $M - N_{200}$  or the  $M - \lambda$  relation. As miscentering and substructure can also contribute to the mismatch problem, we attempt to classify clusters in this sample. The

red dots are clusters with miscentering problems (the offset between X-ray peak and optical center larger than 50 kpc), with most of them representing merging clusters (e.g., Hudson et al. 2010). The blue dots are clusters with projection problems (another nearby X-ray cluster with similar redshift in a 2 Mpc projected radius). The half-red half-blue dots are with both miscentering and projection problems. The black dots are clusters without miscentering and projection

problems. The  $L_X - N$  distribution is similar to the  $T_X - N$  distribution. Similarly, there are more outliers towards lower X-ray luminosity.

Fig. 3 shows the  $Y_X - N$  relation for maxBCG (left panel) and redMaPPer (right panel). The  $Y_X - N$  distribution is similar to the previous two distributions.  $Y_X = M_{gas} \times T_X$  is a robust mass proxy (Kravtsov et al. 2006). The observed large scatter in the  $Y_X - N$  relation reflects the large scatter in the  $M - N$  relation for our sample. The SZ signal  $Y_{SZ}$  is characterized by the integrated Compton parameter  $y_c = \int n_e T_e dl$ . As an X-ray analogue of the integrated Compton parameter,  $Y_X$  is closely related to  $Y_{SZ}$  with a linear relation (Rozo et al. 2014a). Therefore, Fig. 3 may be converted to the  $Y_{SZ} - N$  relation, which also recovers previous stacking results of lower observed SZ signal compared with the model prediction (e.g., Planck Collaboration et al. 2011d; Sehgal et al. 2013; Saro et al. 2017). Moreover, we convert the *Planck* mean stacking  $Y_{SZ}$  (Planck Collaboration et al. 2011d) in the two richest maxBCG bins to the expected  $Y_X$ , using the  $D_A^2 Y_{SZ} - CY_X$  relation (Rozo et al. 2014a; more detail in Appendix A). We also evaluate the observed mean  $Y_X$  (with *XMM-Newton* based  $Y_X$  converted to *Chandra* using the cross-calibration in Appendix B) in the same two bins. The expected  $Y_X$  and observed  $Y_X$  are shown as orange and green bowties in Fig. 3. They are consistent with each other, and both are lower than the model prediction from the combination of X-ray mass proxy with optical weak-lensing mass calibration, which is shown as a solid line.

## 4.2 X-ray scaling relation

Figs. 4 and 5 show the  $L_X - T_X$  relation and the  $L_X - Y_X$  relation for this sample, respectively. Established relations from Vikhlinin et al. (2009a) (*Chandra* calibration) and Pratt et al. (2009) (*XMM-Newton* calibration) are also shown. With the cross-calibration derived in Appendix B, we also rescale all *Chandra* properties to *XMM-Newton*. We find that these optically selected clusters follow the normal  $L_X - T_X$  and  $L_X - Y_X$  relations calibrated from X-ray selected samples. They are not X-ray dark or under-luminous clusters. Instead, many clusters in the sample have optical richness too high for their mass.

## 4.3 X-ray morphology parameters

Besides the dynamical criterion based on the BCG/X-ray offset and cluster environment as presented in Table 3, we also apply several quantitative X-ray morphology parameters in Table 5: the centroid shift ( $w$ ; Mohr et al. 1993), the surface brightness concentration ( $c_{SB}$ ; Santos et al. 2008), and the symmetry-peakiness-alignment (SPA; Mantz et al. 2015). Generally, the  $w$ ,  $s$ , and  $a$  measure the bulk asymmetry, while  $c_{SB}$  and  $p$  judge the CC. The distribution of these parameters are shown in Fig. 6.

# 5 DISCUSSION

## 5.1 Scaling relation from optical, X-ray and SZ

We face two puzzles when we compare the scaling relations from optical, X-ray and SZ observations. The first one is the

mismatch between optical and SZ: the expected SZ signals from the model are higher than the observed ones for stacked optically selected clusters (e.g., Planck Collaboration et al. 2011d; Sehgal et al. 2013; Saro et al. 2017). The second one is the mismatch between optical and X-ray: X-ray selected clusters are more luminous than optically selected clusters (e.g., Gilbank et al. 2004; Dai et al. 2007; Rykoff et al. 2008).

However, the scaling relations between SZ and X-ray are consistent with each other. For example, Planck Collaboration et al. (2011b) extracts the SZ signal individually for the Meta-catalogue of X-ray detected Clusters of galaxies and find that the SZ measurements and the X-ray based predictions are in excellent agreement. Similar results are found based on both X-ray selected clusters (Melin et al. 2011; Planck Collaboration et al. 2011d; Sehgal et al. 2013) and SZ selected clusters (Planck Collaboration et al. 2011a; Planck Collaboration et al. 2011c; Andersson et al. 2011). Moreover even for optically selected clusters, Planck Collaboration et al. (2011d) compares the stacked SZ signal with the stacked ROSAT X-ray luminosity (Rykoff et al. 2008) around maxBCG clusters in the same richness bins and finds the mean SZ signal and mean X-ray luminosity are consistent with the model predictions.

The consistency between SZ and X-ray observations is expected, because they are both from the same ICM. The problem is that optically selected clusters post a challenge for robust stacking of the X-ray or SZ signals.

## 5.2 Possible solutions for the mismatch

As mentioned in Section 1, there are some possible solutions for the mismatch between the stacked *Planck* SZ fluxes and the model expectations for the optically selected clusters. First, we focus on the ICM part to rule out some solutions. The consistency between SZ and X-ray observations demonstrates that the calibration and contamination of the SZ signal are not significantly biased. The assumed pressure profile used to estimate the SZ signal (Arnaud et al. 2010) and the X-ray scaling relation are not significantly biased. These richest maxBCG clusters follow normal  $L_X - T_X$  and  $L_X - Y_X$  relations, which suggests that the fraction of X-ray-dark-but-optical-normal clusters is not significant (at least for massive ones), consistent with some previous studies (e.g., Andreon & Moretti 2011).

Secondly, we focus on galaxies to discuss some remaining solutions. The miscentering (e.g., A1986, A1961) decreases the X-ray luminosity/SZ signal, as some flux moves outside of the aperture. Sehgal et al. (2013) demonstrated the effect of miscentering on decreasing SZ signal. They also proposed that the miscentering effect causes their lower measured SZ signal compared to *Planck* due to the finer resolution of *ACT*. However, as they point out, the miscentering distribution from their sample alone can only explain part of the mismatch between optical and SZ, unless an unrealistic larger offset exists. Moreover, most miscentered clusters are merging or disturbed clusters with lower X-ray or SZ surface brightness, which makes them more difficult to be detected. The discrepancy of SZ signal is at a level of 10% in our richness range (Biesiadzinski et al. 2012). Projection (e.g., A750, A1319) will increase the optical richness. As the cluster mass-richness relation is close to a linear relation, projection causes the projected clusters to simply

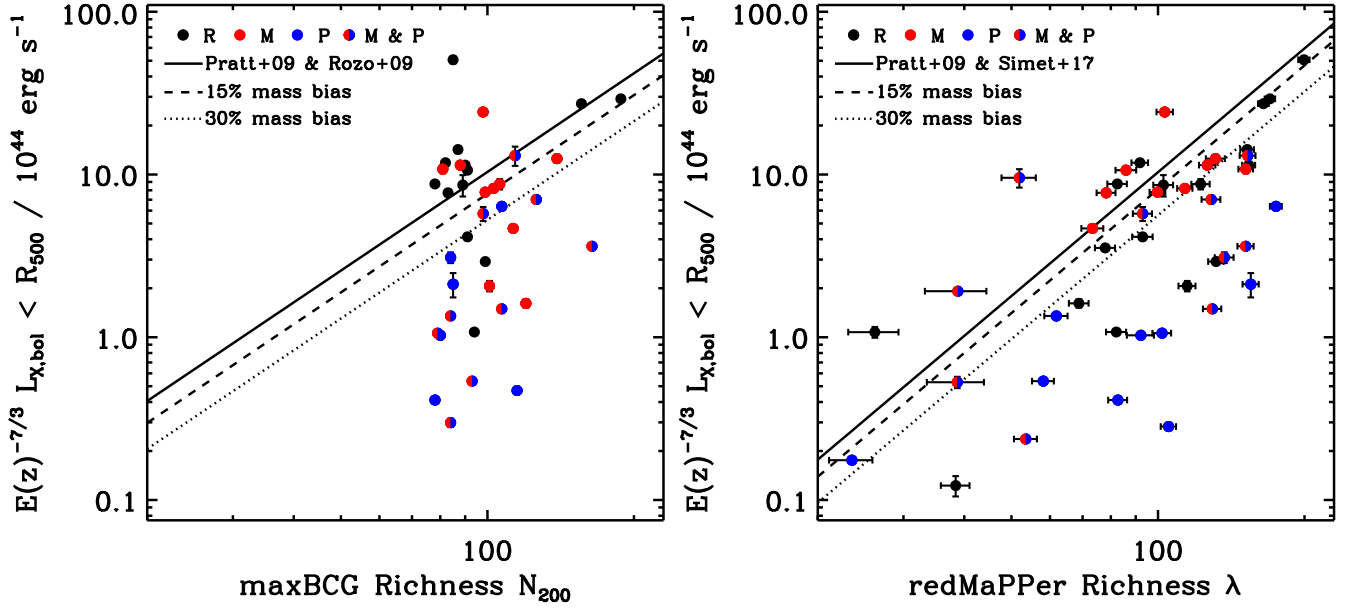


**Figure 2.** *Left:* the bolometric  $L_X - N_{200}$  relation for the sample. Red dots are clusters with Miscentering problems (the offset between the X-ray peak and the optical center larger than 50 kpc), with most of them are merging clusters. Blue dots are clusters with Projection problems (another X-ray cluster within 2 Mpc, which corresponds to 9 arcmin at median redshift = 0.23 for the maxBCG sample, comparable to *Planck*’s resolution). Half-red half-blue dots are clusters with both Miscentering and Projection problems. Black dots are Relaxed clusters without miscentering and projection problems. The solid line shows the expected  $L_X - N_{200}$  relation from the X-ray  $L_X - M$  relation (Pratt et al. 2009) and the weak-lensing  $M - N_{200}$  relation (Rozo et al. 2009) on the full maxBCG sample (Appendix A). The dashed line and the dotted line show 15% and 30% hydrostatic bias respectively. *Right:*  $L_X - \lambda$  relation for the sample. The  $L_X - M$  relation (Pratt et al. 2009) and the  $M - \lambda$  relation (Simet et al. 2017) are combined. These two plots show the roles of miscentering and projection on the scatter of the optical richness relations, while the cluster mass bias can also reduce the mismatch.

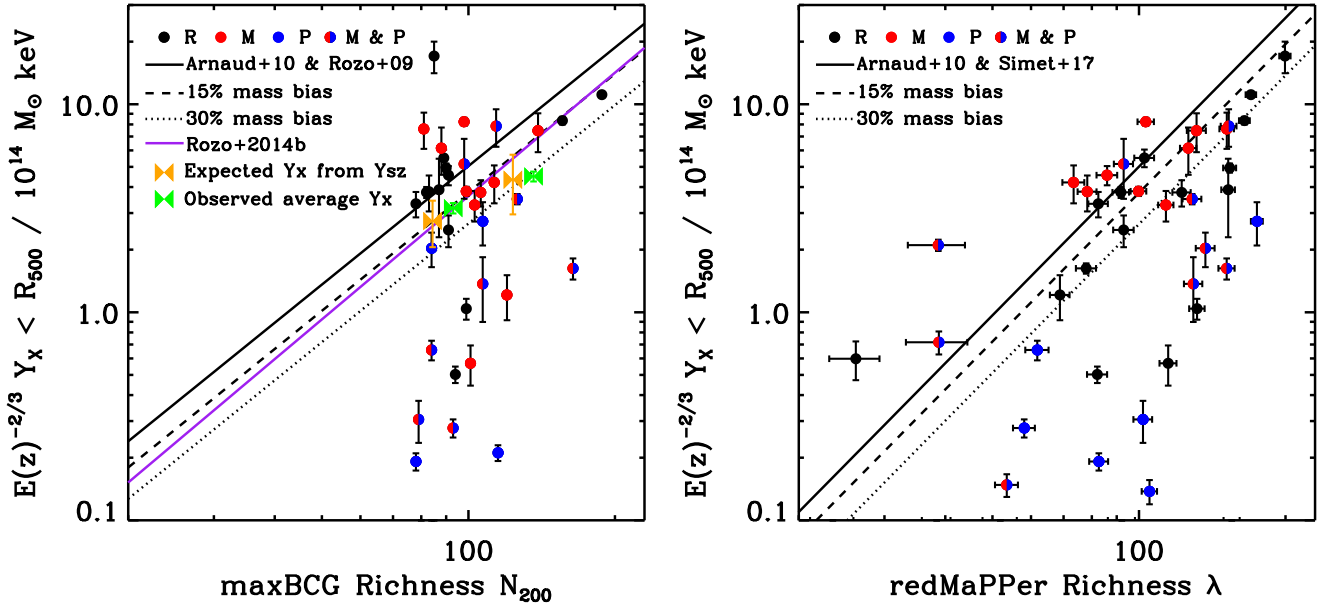


**Figure 3.** The relations between  $Y_X$  and the optical richness for the sample, with the same symbol set as in Fig. 2. Orange bowties are the expected  $Y_X$ , which is inferred from the *Planck* mean stacking  $Y_{SZ}$  in the two richest maxBCG bins (Planck Collaboration et al. 2011d). The  $D^2_{Y_{SZ}} - CY_X$  relation from Rozo et al. (2014a) is assumed. Green bowties are the observed mean  $Y_X$  in the same two bins. The bowties are misplaced to the average richness of each bin to avoid overlapping. The expected  $Y_X$  and observed  $Y_X$  are consistent with each other, and both of them are lower than the model prediction shown by the solid line. The black solid line combines the  $M - Y_X$  relation (Arnaud et al. 2010) and the  $M - N_{200}$  relation (Rozo et al. 2009) on the full maxBCG sample (Appendix A) for the *Left*, and the  $M - Y_X$  relation (Arnaud et al. 2010) and the  $M - \lambda$  relation (Simet et al. 2017) for the *Right*. We also plot the predicted  $Y_X - N_{200}$  from Rozo et al. (2014b) as a purple line in the left panel. Most relaxed clusters are close to the expected scaling relation.

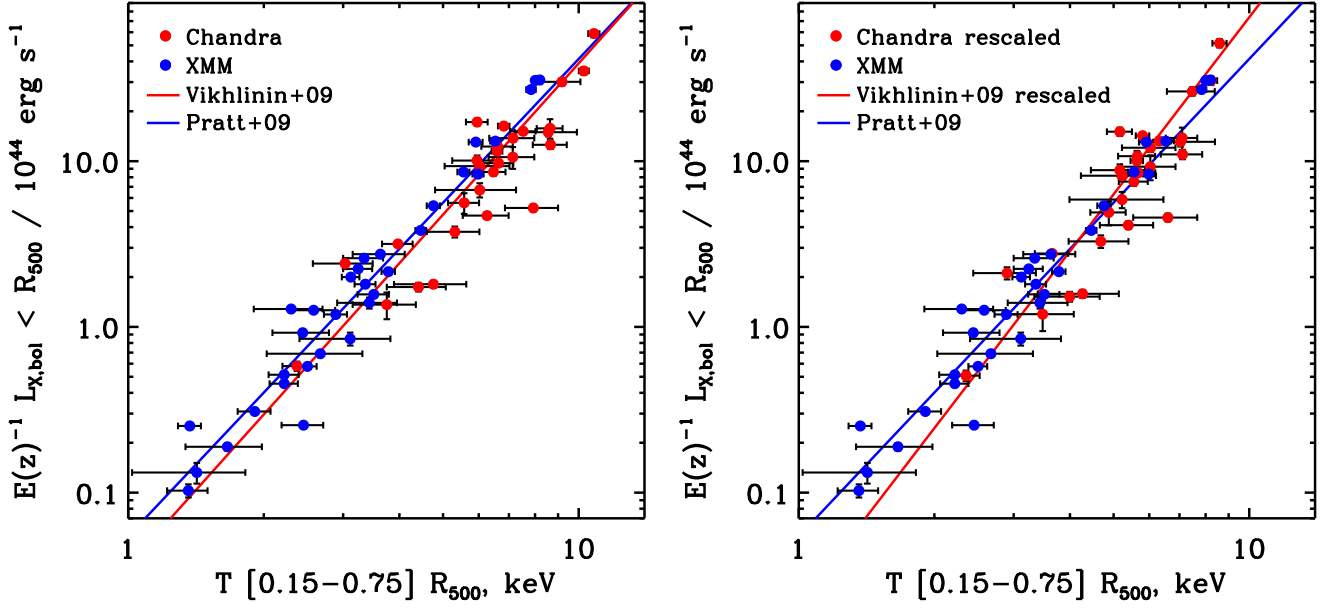


**Figure 4.** Left: the  $L_X - T_X$  relation for individual clusters from Table 3 (red: *Chandra*, blue: *XMM-Newton*). The red line is the  $L_X - T_X$  relation (Vikhlinin et al. 2009a) based on *Chandra* calibration, while the blue line (Pratt et al. 2009) is based on *XMM-Newton* calibration. Right: *Chandra* data ( $L_X$  and  $T_X$ ) and  $L_X - T_X$  relation are rescaled to *XMM-Newton* with the in-house cross-calibration in Appendix B. These clusters follow the normal  $L_X - T_X$  relation with less scatters than those in Fig. 2.

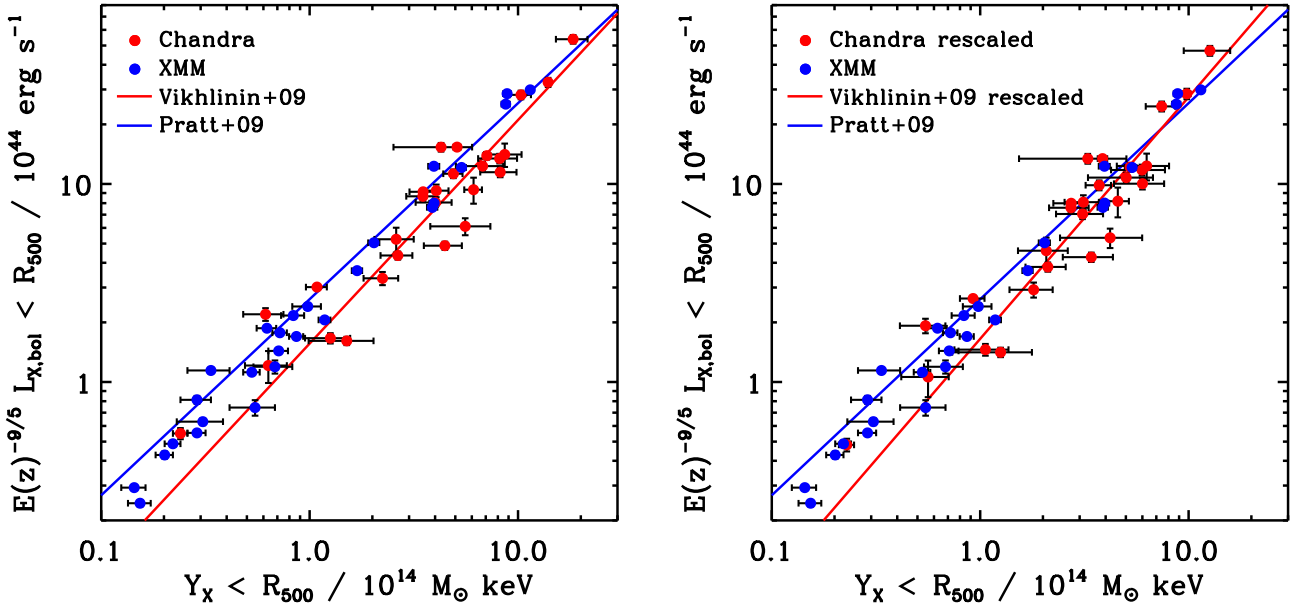


**Figure 5.** Left: the  $L_X - Y_X$  relation for individual clusters from Table 3. The red line is the  $L_X - Y_X$  relation (Vikhlinin et al. 2009a) based on *Chandra* calibration, while the blue line (Pratt et al. 2009) is based on *XMM-Newton* calibration. Right: *Chandra* data ( $L_X$  and  $Y_X$ ) and  $L_X - Y_X$  relation are rescaled to *XMM-Newton* with the in-house cross-calibration in Appendix B. These clusters follow the normal  $L_X - Y_X$  relation with less scatters than those in Fig. 2.

slide up and down the mass-richness relation, without deviating from it (Simet et al. 2017). However, the  $L_X - M$  or  $Y_{SZ} - M$  relation is a power-law relation with an index greater than one ( $\sim 1.6$ ; Rozo et al. 2014a). For example, if we have two clusters with  $N_{200} = 80$  ( $M_{500|N=80} = 5.5 \times 10^{14} M_\odot$ , bolometric X-ray luminosity  $L_{X|N=80} = 13 \times 10^{44} \text{ erg s}^{-1}$ ) projected together, they will be detected as a  $N=160$  clus-

ter ( $M_{500|N=160} = 11 \times 10^{14} M_\odot$ ,  $L_{X|N=160} = 48 \times 10^{44} \text{ erg s}^{-1}$ ). Though the mass is equal to the sum of two subclusters, the total X-ray luminosity is overestimated by a factor of  $\sim 2$ . Thus, projection causes the expected X-ray luminosity or the SZ signal from the summed optical richness to be higher than the actual summed values. The projection fraction is around 10% (Simet et al. 2017), even higher for these richest



maxBCG clusters (Fig. 2). The above two effects can act together, especially in super clusters and large-scale filaments (Fig. D1). We also note that there is contamination of low  $L_X$  systems. For example, there are 4 low  $L_X$  systems beyond the  $2\sigma$  line of  $L_X - N$  relation from Rozo et al. (2014b) in Fig. A2 (and 7 beyond the  $1.5\sigma$  line towards lower  $L_X$  vs. 1 beyond the  $1.5\sigma$  line towards higher  $L_X$ ), although it tends to disappear with increasing mass bias. Taking these numbers at face value, the contamination is 10% - 15%.

Thirdly, the mismatch may be induced by the mass bias and covariance bias between the ICM and galaxy scaling relations. The mass bias is either from the X-ray HE mass or the lensing mass. Rozo et al. (2014b) found the mismatch problem could be solved by lowering the galaxy weak-lensing mass by 10% while raising the X-ray mass by 21%. The weak-lensing mass could be overestimated due to line-of-sight (LOS) contamination and triaxial halo (e.g., Corless & King 2007). The red-sequence cluster finding algorithm tends to find more prolate clusters (major axis aligned with LOS) than oblate clusters due to higher galaxy density and background contrast. This orientation bias can lead to 3-6% overestimate of lensing mass (Dietrich et al. 2014). The covariance bias between  $M_{wl}$  and  $N$  at fixed mass can also induce a 10% overestimate of lensing mass (Eq. 12 of Rozo et al. 2014b and Appendix A). We overplot the cluster mass estimated from the galaxy velocity dispersion (Farahi et al. 2016) in the right panel of Fig. 1, and also compare with results from CMB weak-lensing (Geach & Peacock 2017; Baxter et al. 2018). Indeed the galaxy weak-lensing mass is higher than the mass from the other two methods, although uncertainty with the latter two relations is substantial. Meanwhile, the X-ray HE mass could be underestimated due to gas bulk motion and turbulence (e.g., Nagai et al. 2007; Lau et al. 2009). We also overplot the 15% or 30% HE bias as dashed or dotted lines in Figs. 1 left panel, 2, and 3. The 30% HE is approximately equivalent to the 21% HE bias with 10% weak-lensing bias, which reduces the mismatch. Thus the combination of weak-lensing and X-ray HE bias can also contribute to reduce the mismatch. Moreover, the covariance bias from the multivariate scaling relations (Appendix A) leads an additional  $\sim 10\%$  correction.

### 5.3 Can we further increase the robustness of the optical richness

From the ICM-galaxy scaling relations, we find that optically selected clusters have large scatter with more clusters biased to lower mass. Both Planck Collaboration et al. (2011d) and Sehgal et al. (2013) selected a BCG-dominated subsample of their optically selected clusters, defined as the BCG luminosity ratio  $L_{BCG}/(L_{tot} - L_{BCG})$ , being larger than the average ratio for a given richness bin. They find that the BCG-dominated sample has a higher normalization, closer to the predicted relation.

Planck Collaboration et al. (2013) compared the scaling relation between the SZ signal and the stellar mass for a large sample of locally brightest galaxies, analogous to a BCG-dominated sample. The relation is close to the self-similar prediction extending from rich clusters down to groups ( $M_{500} \sim 2 \times 10^{13} M_\odot$ ), but with a normalization  $\sim 20\%$  lower than the X-ray selected clusters. This mismatch is mainly from the Malmquist bias from the X-ray sample and

the miscentering from satellite contamination (Planck Collaboration et al. 2013). Meanwhile, Hand et al. (2011) and Greco et al. (2015) found consistent results, at least down to the group mass scale (but necessarily to the lower mass systems). Moreover, Gralla et al. (2014) found that the stacked SZ signal from radio selected sources is also consistent with the self-similar prediction. The SZ signal is mainly from the AGN hosted halos of giant galaxies instead of galaxy clusters or groups. The miscentering and projection problems are insignificant for such giant galaxies compared with the massive optically selected clusters.

We also select a BCG-dominated subsample with the maxBCG and redMaPPer catalogues locating the same BCG. Fig. A1 shows that the BCG-dominated clusters tend to be relaxed clusters and agree better with the model prediction than the full sample. Three of the four low luminosity outliers have the projection problems (see Fig. 2). Therefore, the BCG-dominated subsample more closely correspond to the X-ray selected and SZ selected samples.

### 5.4 Dynamical state and cool core fraction

As an optically selected sample, this sample also provides an opportunity to study the ICM dynamical state and cool core (CC) fraction using the X-ray morphology parameters presented in § 4.3, without any ICM selection bias. Due to the diversity in the recent merger histories of individual clusters, which is further complicated by projection, the morphological parameters should be treated with caution. However, they provide useful statistical tools to characterise trends of properties in large cluster samples (e.g., Böhringer et al. 2010). We use  $w$  and  $c_{SB}$  to compare the fractions of relaxed ( $w \leq 0.01$ ) and CC ( $c_{SB} \geq 0.075$ ) clusters among optical, SZ, and X-ray selected samples (Table 6). Both the fractions of relaxed and CC clusters change as: optical < SZ < X-ray. Moreover, the combination of asymmetry and CC indicators provide a more rigorous definition for relaxed clusters, e.g., the SPA criterion ( $s > 0.87$ ,  $p > -0.82$ , and  $a > 1.00$ ; Mantz et al. 2015). Only 1 out of 55 clusters in our sample (2%) is close to the SPA criterion, compared with 57/361 (16%) for an X-ray selected sample (Mantz et al. 2015). Simulations also tend to find less relaxed clusters compared with an X-ray selected sample (e.g., Böhringer et al. 2010).

## 6 CONCLUSIONS

Great progress on galaxy clusters has been made in the last decade with X-ray, SZ and optical surveys. The scaling relations between X-ray and SZ are consistent with each other for X-ray, SZ and even optically selected clusters, because both the X-ray emission and SZ signal are from the same ICM. However, mismatches emerge when we compare the ICM scaling relation based on X-ray and SZ data with the galaxy scaling relation based on optical data.

In order to study the mismatch problem, we directly compare the optical and X-ray scaling relations for a complete sample of 38 richest maxBCG clusters.  $T_X - N$ ,  $L_X - N$ ,  $Y_X - N$  relations show large scatter with more outliers towards lower  $T_X$ ,  $L_X$  or  $Y_X$ . On the other hand, these clusters follow normal  $L_X - T_X$  and  $L_X - Y_X$  relations. We list

**Table 5.** X-ray morphological parameters

Cluster	$w$	$c_{\text{SB}}$	$s$	$p$	$a$
A2142	$0.007 \pm 0.001$	$0.075 \pm 0.001$	$0.788 \pm 0.014$	$-0.921 \pm 0.005$	$1.159 \pm 0.017$
J150M	$0.011 \pm 0.005$	$0.054 \pm 0.010$	$0.843 \pm 0.179$	$-1.259 \pm 0.323$	$0.870 \pm 0.308$
J150E	$0.025 \pm 0.008$	$0.050 \pm 0.015$	$0.772 \pm 0.196$	$-1.596 \pm 0.412$	$0.663 \pm 0.284$
J150W	$0.026 \pm 0.011$	$0.031 \pm 0.014$	$0.475 \pm 0.218$	$-1.694 \pm 0.697$	$0.280 \pm 0.240$
A1689	$0.002 \pm 0.001$	$0.116 \pm 0.002$	$1.166 \pm 0.053$	$-0.829 \pm 0.018$	$1.423 \pm 0.035$
A1443	$0.037 \pm 0.010$	$0.025 \pm 0.003$	$0.650 \pm 0.164$	$-1.501 \pm 0.142$	$0.789 \pm 0.090$
A781	$0.046 \pm 0.002$	$0.023 \pm 0.002$	$0.446 \pm 0.023$	$-1.881 \pm 0.825$	$0.941 \pm 0.032$
A781M	$0.007 \pm 0.002$	$0.029 \pm 0.004$	$1.172 \pm 0.150$	$-1.772 \pm 0.349$	$1.203 \pm 0.220$
A781E	$0.009 \pm 0.003$	$0.020 \pm 0.005$	$1.181 \pm 0.216$	$-1.770 \pm 0.492$	$1.381 \pm 0.326$
A781W	$0.010 \pm 0.003$	$0.073 \pm 0.007$	$0.966 \pm 0.151$	$-1.158 \pm 0.071$	$1.030 \pm 0.180$
A1986	$0.019 \pm 0.005$	$0.047 \pm 0.010$			
A1882E	$0.024 \pm 0.005$	$0.051 \pm 0.004$	$0.575 \pm 0.091$	$-1.843 \pm 0.540$	$0.995 \pm 0.221$
A1882W	$0.020 \pm 0.005$	$0.051 \pm 0.010$	$0.552 \pm 0.238$	$-1.674 \pm 0.274$	$0.137 \pm 0.234$
A1882M	$0.012 \pm 0.005$	$0.271 \pm 0.041$	$0.883 \pm 0.150$	$-0.895 \pm 0.036$	$0.819 \pm 0.209$
A1882N	$0.034 \pm 0.011$	$0.058 \pm 0.016$			
A1758N	$0.026 \pm 0.019$	$0.016 \pm 0.005$	$0.517 \pm 0.240$	$-1.604 \pm 0.281$	$1.438 \pm 0.090$
A1758S	$0.015 \pm 0.001$	$0.041 \pm 0.002$	$0.497 \pm 0.034$	$-1.376 \pm 0.402$	$0.971 \pm 0.053$
A1760	$0.029 \pm 0.005$	$0.037 \pm 0.007$			
A1622	$0.036 \pm 0.001$	$0.046 \pm 0.001$			
A750E	$0.007 \pm 0.001$	$0.075 \pm 0.003$	$1.021 \pm 0.098$	$-1.086 \pm 0.022$	$1.298 \pm 0.072$
A750W	$0.042 \pm 0.004$	$0.056 \pm 0.006$	$0.178 \pm 0.056$	$-1.172 \pm 0.208$	$0.827 \pm 0.274$
A1682	$0.034 \pm 0.006$	$0.039 \pm 0.005$	$0.429 \pm 0.072$	$-1.414 \pm 0.332$	$0.444 \pm 0.140$
A1246	$0.011 \pm 0.004$	$0.047 \pm 0.007$	$0.671 \pm 0.214$	$-1.265 \pm 0.111$	$0.745 \pm 0.291$
A1961	$0.026 \pm 0.008$	$0.051 \pm 0.013$	$0.564 \pm 0.124$	$-1.496 \pm 0.798$	$0.624 \pm 0.231$
A2034	$0.015 \pm 0.002$	$0.027 \pm 0.001$	$0.904 \pm 0.039$	$-1.316 \pm 0.081$	$0.911 \pm 0.035$
A655	$0.018 \pm 0.006$	$0.047 \pm 0.005$	$0.466 \pm 0.144$	$-1.427 \pm 0.147$	$0.774 \pm 0.236$
A1914	$0.010 \pm 0.001$	$0.061 \pm 0.002$	$0.660 \pm 0.034$	$-1.000 \pm 0.014$	$1.352 \pm 0.069$
Z5247	$0.056 \pm 0.013$	$0.029 \pm 0.006$	$0.530 \pm 0.149$	$-1.767 \pm 0.673$	$1.247 \pm 0.319$
A657	$0.011 \pm 0.003$	$0.114 \pm 0.007$	$0.571 \pm 0.104$	$-1.073 \pm 0.083$	$0.638 \pm 0.187$
J229	$0.012 \pm 0.003$	$0.061 \pm 0.006$	$1.148 \pm 0.195$	$-1.607 \pm 0.517$	$1.100 \pm 0.289$
A2051	$0.012 \pm 0.001$	$0.050 \pm 0.003$	$0.718 \pm 0.074$	$-1.349 \pm 0.212$	$1.001 \pm 0.114$
A2051S	$0.009 \pm 0.005$	$0.105 \pm 0.019$	$0.888 \pm 0.291$	$-1.353 \pm 0.264$	$1.084 \pm 0.455$
A2051N	$0.015 \pm 0.005$	$0.069 \pm 0.009$	$0.480 \pm 0.138$	$-2.324 \pm 1.295$	$0.757 \pm 0.374$
A2050	$0.011 \pm 0.001$	$0.052 \pm 0.002$	$0.777 \pm 0.050$	$-1.230 \pm 0.072$	$1.335 \pm 0.126$
A1423	$0.007 \pm 0.004$	$0.101 \pm 0.008$	$1.005 \pm 0.111$	$-1.003 \pm 0.036$	$1.034 \pm 0.122$
A801	$0.014 \pm 0.004$	$0.082 \pm 0.009$	$0.772 \pm 0.153$	$-1.141 \pm 0.066$	$0.863 \pm 0.186$
A773	$0.007 \pm 0.002$	$0.045 \pm 0.003$	$1.147 \pm 0.115$	$-1.185 \pm 0.052$	$1.264 \pm 0.082$
A1576	$0.017 \pm 0.004$	$0.048 \pm 0.005$	$0.805 \pm 0.097$	$-1.138 \pm 0.051$	$1.021 \pm 0.081$
A2631	$0.030 \pm 0.004$	$0.033 \pm 0.003$	$0.636 \pm 0.083$	$-1.282 \pm 0.123$	$0.988 \pm 0.077$
A1703	$0.014 \pm 0.003$	$0.047 \pm 0.003$	$0.830 \pm 0.166$	$-1.130 \pm 0.046$	$1.396 \pm 0.080$
A2219	$0.007 \pm 0.001$	$0.027 \pm 0.001$	$1.008 \pm 0.073$	$-1.159 \pm 0.033$	$1.442 \pm 0.051$
A1319M	$0.013 \pm 0.006$	$0.070 \pm 0.022$			
A1319NW	$0.022 \pm 0.009$	$0.089 \pm 0.018$			
A1560	$0.065 \pm 0.007$	$0.060 \pm 0.007$			
J175N	$0.023 \pm 0.014$	$0.043 \pm 0.014$			
J175S	$0.017 \pm 0.006$	$0.051 \pm 0.015$			
J249SW	$0.014 \pm 0.004$	$0.039 \pm 0.006$	$0.751 \pm 0.125$	$-1.586 \pm 0.399$	$1.288 \pm 0.218$
J249NE	$0.009 \pm 0.004$	$0.072 \pm 0.010$	$0.907 \pm 0.249$	$-1.476 \pm 0.566$	$0.792 \pm 0.360$
A1201	$0.023 \pm 0.001$	$0.100 \pm 0.002$	$0.539 \pm 0.048$	$-1.034 \pm 0.022$	$0.696 \pm 0.119$
A2009	$0.003 \pm 0.001$	$0.163 \pm 0.007$	$1.141 \pm 0.141$	$-0.894 \pm 0.026$	$1.381 \pm 0.088$
A2111	$0.043 \pm 0.014$	$0.040 \pm 0.004$	$0.495 \pm 0.108$	$-1.479 \pm 0.567$	$0.792 \pm 0.051$
A815	$0.027 \pm 0.012$	$0.020 \pm 0.005$			
Z1450	$0.009 \pm 0.003$	$0.036 \pm 0.009$	$0.878 \pm 0.151$	$-1.525 \pm 0.158$	$0.799 \pm 0.240$
A1765	$0.005 \pm 0.002$	$0.065 \pm 0.009$	$0.908 \pm 0.228$	$-1.604 \pm 0.629$	$0.897 \pm 0.400$
A1902	$0.008 \pm 0.003$	$0.148 \pm 0.009$	$0.796 \pm 0.135$	$-0.939 \pm 0.020$	$0.897 \pm 0.172$

Note. The centroid shift ( $w$  within  $R_{500}$ , [Mohr et al. 1993](#)), the surface brightness concentration ( $c_{\text{SB}}$  in 40-400 kpc range; [Santos et al. 2008](#)), and the symmetry-peakiness-alignment (SPA; [Mantz et al. 2015](#)).

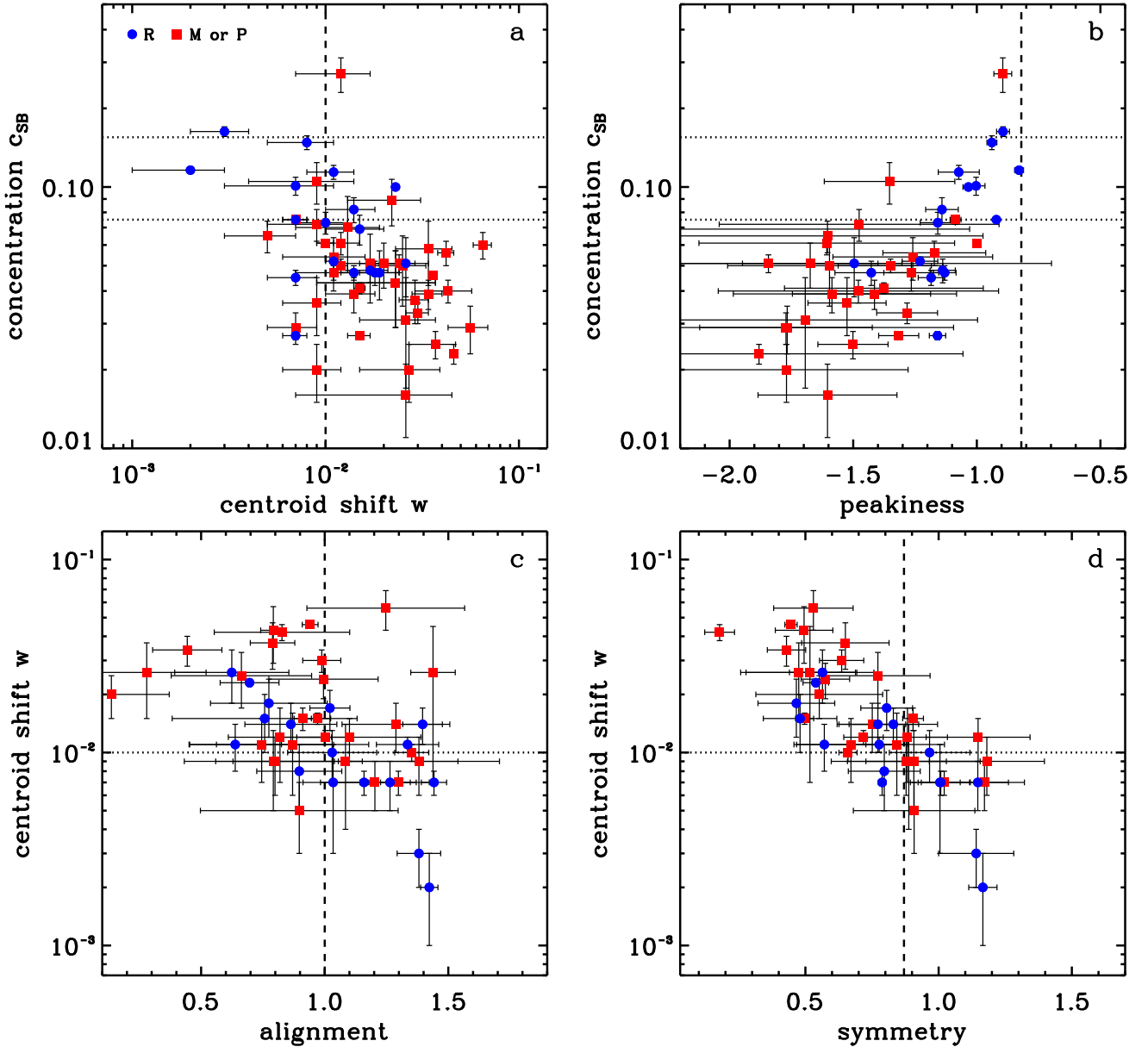


**Figure 6.** The distribution of X-ray morphology parameters. Red squares are disturbed clusters with the same miscentering and projection problems as in Figs. 2 and 3, while blue dots are relaxed clusters without miscentering and projection problems. The lines mark the classification threshold:  $w \leq 0.01$  for relaxed clusters;  $c_{SB} \geq 0.075$  for moderate CC clusters and  $c_{SB} \geq 0.155$  for pronounced CC clusters;  $s > 0.87$ ,  $p > -0.82$ , and  $a > 1.00$  for relaxed clusters. The CC indicators  $c_{SB}$  and  $p$  are correlated with each other. The asymmetry indicators  $w$ ,  $s$ , and  $a$  are also correlated.

these factors contributing to the mismatches: (1) miscentering,  $\sim 10\%$ ; (2) projection,  $\sim 10\%$ ; (3) contamination of low mass systems of optical selection,  $\sim 10\% - 15\%$ ; (4) hydrostatic mass bias,  $\sim 10\% - 30\%$ ; (5) weak-lensing mass bias,  $\sim 10\%$ ; and (6) covariance bias,  $\sim 10\%$ . These biases mix in some cases and can compensate with each other, but the dominant one is likely the mass bias, e.g., 30% mass bias induce a 50% decrement of SZ signal assuming  $Y_{SZ} \propto N^{1.9}$ . More studies are required to constrain these biases better.

This optically selected sample also provides an unbiased perspective to the ICM properties. We find a rising fraction

of relaxed or CC clusters from optical ( $\sim 26\%$ ), to SZ ( $\sim 36\%$ ), and to X-ray ( $\sim 61\%$ ) selected samples.

Optical surveys and algorithms are very successful and efficient for finding clusters, but the mass proxies from optical methods like the maxBCG  $N_{200}$  still have large scatter. Our results may suggest a bias for the optically richest clusters, which should be noted and corrected in future analyses. In the future, one has to apply a more robust optical mass proxy to reduce the bias from optical selection, such as the redMaPPer  $\lambda$  or the velocity dispersion from the upcoming Dark Energy Spectroscopic Instrument (DESI) survey, and meanwhile develop accurate mass calibrations with the

**Table 6.** The fractions of relaxed and CC clusters

	optical	SZ	X-ray
Relaxed ( $w \leq 0.01$ )	29% (55 <sup>a</sup> )	35% (120 <sup>b</sup> )	61% (31 <sup>c</sup> )
CC ( $c_{\text{SB}} \geq 0.075$ )	22% (55 <sup>a</sup> )	36% (164 <sup>d</sup> )	61% (100 <sup>d</sup> )

*Note.* <sup>a</sup>This work from Table 5, the number in brackets is the total cluster number in the sample. <sup>b</sup>Lovisari et al. (2017). <sup>c</sup>Böhringer et al. (2010). <sup>d</sup>Andrade-Santos et al. (2017). This optically selected sample shows lower fractions of relaxed and CC clusters compared with SZ and X-ray selected samples.

aid of simulations, before we implement the resulting scaling relations to study cosmology.

## ACKNOWLEDGEMENTS

Support for this work was provided by the National Aeronautics and Space Administration grants NNX16AH32G and NNX16AH26G. Support for this work was also provided by the National Aeronautics and Space Administration through *Chandra* Award Number GO4-15119B and GO4-15115X issued by the *Chandra* X-ray Center, which is operated by the Smithsonian Astrophysical Observatory for and on behalf of the National Aeronautics Space Administration under contract NAS8-03060. ER is supported by DOE grant DE-SC0015975 and by the Sloan Foundation, grant FG-2016-6443. NS acknowledges support from NSF grant 1513618. DN acknowledges support from NSF grant AST-1412768. This research has made use of data and/or software provided by the High Energy Astrophysics Science Archive Research Center (HEASARC), which is a service of the Astrophysics Science Division at NASA/GSFC and the High Energy Astrophysics Division of the Smithsonian Astrophysical Observatory.



## APPENDIX A: MULTIVARIATE SCALING RELATIONS

Due to the slope or asymmetry of the mass function and the mass variance, the mean of the correlated multivariate scaling relation is not equal to the naive ‘plug in’ expectation (e.g., Allen et al. 2011; Evrard et al. 2014). Following Rozo et al. (2014a), we define  $m = \ln(M/M_0)$  and the mean distribution of log-observable, e.g., temperature  $t = \ln(T_X/T_{X,0})$ , is

$$\langle t|m \rangle = a_{t|m} + s_{t|m}m, \quad (\text{A1})$$

where  $a_{t|m}$  is the amplitude and  $s_{t|m}$  is the slope of scaling relation. Using Bayes Theorem, we can convert the  $T_X - M$  relation to  $M - T_X$  relation with the Eq. A5 of Rozo et al. (2014a),

$$\langle m|t \rangle = \left[ \frac{t - a_{t|m}}{s_{t|m}} \right] - \beta \sigma_{m|t}^2, \quad (\text{A2})$$

The first term in square brackets is the naive expected mean from Eq. A1, while the second term is the Eddington bias correction.  $\beta$  is the slope of the halo mass function ( $dn/d \ln M \propto M^{-\beta}$ ) and  $\sigma_{m|t}$  is the scatter in  $m$  at fixed  $t$ . Assuming the Tinker et al. (2008) mass function and the WMAP9 cosmology (Hinshaw et al. 2013), in the mass range of this sample ( $0.6 - 13.3 \times 10^{14} M_\odot$ ),  $\beta = 1.4 - 4.5$ .

**$L_X - N$  relation** is derived from the  $L_X - M$  relation (Pratt et al. 2009;  $L_1 - M_Y$  MB in Table 2) and the  $M - N$  relation (Rozo et al. 2009; Simet et al. 2017) using Eq. A13 of Rozo et al. (2014a),

$$\langle l|n \rangle = a_{l|m} + s_{l|m}(\langle m|n \rangle + r\beta\sigma_{m|l}\sigma_{m|n}). \quad (\text{A3})$$

Thus the amplitude and slope of  $L_X - N$  relation are

$$a_{l|n} = [a_{l|m} + s_{l|m}a_{m|n}] + r_{l,n|m}\beta s_{l|m}\sigma_{m|l}\sigma_{m|n}, \quad (\text{A4})$$

$$s_{l|n} = s_{l|m}s_{m|n}. \quad (\text{A5})$$

On the amplitude, the term in square brackets is the naive ‘plug in’ value. The other term is the covariance bias,  $r_{l,n|m}$  is the correlation coefficient between  $l$  and  $n$  at fixed  $m$ . We note the binned masses of Rozo et al. (2009) and Simet et al. (2017) measure the  $\ln \langle M|N \rangle$  rather than  $\langle \ln M|N \rangle$ , and  $\ln \langle M|N \rangle = \langle \ln M|N \rangle + \frac{1}{2}\sigma_{m|n}^2$  assuming a log-normal distribution, thus the amplitude is related as  $\tilde{a}_{m|n} = a_{m|n} + \frac{1}{2}\sigma_{m|n}^2$ . We quote their  $\tilde{a}_{m|n}$  and get  $a_{m|n}$  by subtracting  $\frac{1}{2}\sigma_{m|n}^2$ . To get an order of magnitude estimate for the bias term, we set  $\beta = 2.8$ . To the first order, the hot gas - galaxy correlation coefficient is zero, which results in no bias. However, recent studies suggest negative hot gas - galaxy correlation and we also take  $r_{l,n|m} = -0.3$  (Farahi et al. 2017 & private communication with Gus Evrard) to examine its impact. We also apply  $\sigma_{m|l} = 0.28$  (Angulo et al. 2012) and  $\sigma_{m|n} = 0.45$  (Rozo et al. 2009) or  $\sigma_{m|\lambda} = 0.25$  (Rozo & Rykoff 2014), which yields a correction term  $\sim -0.20$  ( $\sim -0.11$  for  $\lambda$ ), corresponds to a 18% (11%) down offset for the amplitude of  $L_X$ . If we set  $\beta$  in the range of 1.4 – 4.5, the down offset is 10% – 28% (5% – 16% for  $\lambda$ ) instead. Fig. A1 compares the difference between the ‘plug in’ method and the bias corrected method with different  $\beta$  values for the maxBCG

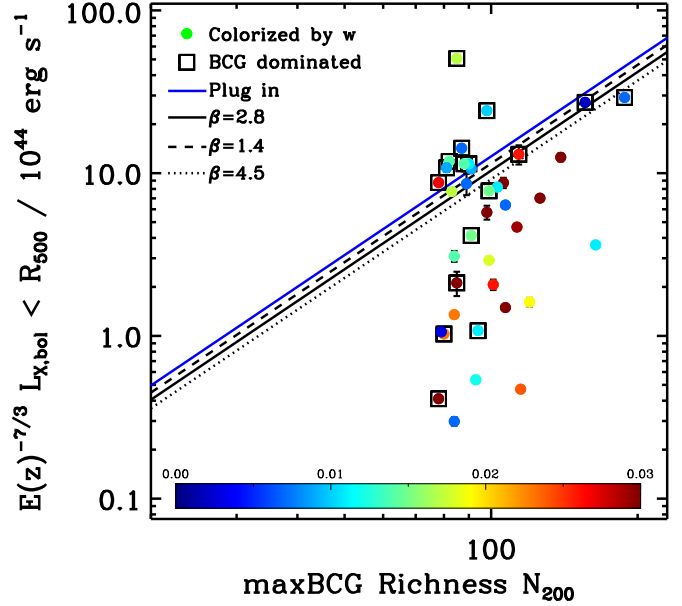


**Figure A1.** Comparison of the ‘plug in’  $L_X - N_{200}$  relation (blue solid line) with the bias corrected ones. The ‘plug in’ relation simply combines the X-ray  $L_X - M$  relation (Pratt et al. 2009) and the weak-lensing  $M - N_{200}$  relation (Rozo et al. 2009). The black solid, dashed, and dotted lines show bias corrected relation for  $\beta$  of 2.8, 1.4, and 4.5, respectively. The dots are colored by the centroid shift  $w$ . The black boxes represent a BCG dominated subsample with the maxBCG and redMaPPer locating the same galaxy as the BCG (see Section 5.3). The BCG dominated clusters tend to be relaxed clusters and follow more closely to the model prediction of solid line.

sample. In order to compare with previous publications, especially the ones from *ROSAT*, we also present the  $L_X$  in 0.1–2.4 keV in Fig. A2. The  $L_{0.1-2.4\text{keV}}$  is converted from  $L_{X,bol}$  using an *apec* model with metallicity fixed to  $0.3Z_\odot$ . The black line is the predicted  $L_X - N$  relation from the  $L_X - M$  relation (Pratt et al. 2009;  $L_{[0.1-2.4]} - M_Y$  MB in Table B2) and the  $M - N$  relation (Rozo et al. 2009) using Eqs. A4 and A5. The purple line is from the preferred  $L_X - N$  relation (Rozo et al. 2014b; Table 4).

**$T_X - N$  relation** is derived from the  $M - T_X$  relation (Sun et al. 2009; Tier 1 + 2-clusters in Table 6) and the  $M - N$  relation (Rozo et al. 2009; Simet et al. 2017). From Eq. A13 of Rozo et al. (2014a), we find

$$\langle t|n \rangle = a_{t|m} + s_{t|m}(\langle m|n \rangle + r_{t,n|m}\beta\sigma_{m|t}\sigma_{m|n}) \quad (\text{A6})$$

The  $M - T_X$  relation is related to the  $T_X - M$  relation from Eq. A2,

$$a_{t|m} = -\frac{a_{m|t} + \beta\sigma_{m|t}^2}{s_{m|t}}, \quad s_{t|m} = \frac{1}{s_{m|t}}, \quad (\text{A7})$$

substitute  $a_{t|m}$  and  $s_{t|m}$  into Eq. A6, we get the amplitude and slope of  $T_X - N$  relation as

$$a_{t|n} = \left[ \frac{a_{m|n} - a_{m|t}}{s_{m|t}} \right] + \frac{\beta\sigma_{m|t}}{s_{m|t}}(r_{t,n|m}\sigma_{m|n} - \sigma_{m|t}), \quad (\text{A8})$$

$$s_{t|n} = \frac{s_{m|n}}{s_{m|t}}. \quad (\text{A9})$$

We assume  $r_{t,n|m} = -0.3$  (Farahi et al. 2017 & private communication with Gus Evrard) and  $\sigma_{m|t} = 0.20$  (Kravtsov et al. 2006) to estimate the bias, which yields a correction term of  $\sim -0.10$ , corresponding to a 10% down offset for  $n$  or  $\lambda$ .

**$Y_X - N$  relation** is derived from the  $M - Y_X$  relation (Arnaud et al. 2010; Eq. 2) and the  $M - N$  relation (Rozo et al. 2009; Simet et al. 2017) as:

$$a_{x|n} = \left[ \frac{a_{m|n} - a_{m|x}}{s_{m|x}} \right] + \frac{\beta \sigma_{m|x}}{s_{m|x}} (r_{x,n|m} \sigma_{m|n} - \sigma_{m|x}), \quad (\text{A10})$$

$$s_{x|n} = \frac{s_{m|n}}{s_{m|x}}. \quad (\text{A11})$$

Assuming  $r_{x,n|m} = -0.2$  (Farahi et al. 2017 & private communication with Gus Evrard) and  $\sigma_{m|x} = 0.087$  (Arnaud et al. 2010), we derive a correction term of  $\sim -0.07$ , corresponding to a 7% down offset for  $n$  or  $\lambda$ .

**$Y_X - N$  relation** is also from the  $Y_{SZ} - Y_X$  relation (Rozo et al. 2014a; M10 data set in Table 1) and the  $Y_{SZ} - N$  relation (Rozo et al. 2014b; Table 4) as:

$$a_{x|n} = \left[ \frac{a_{sz|n} - a_{sz|x}}{s_{sz|x}} \right] + \frac{\beta \sigma_{sz|x}}{s_{sz|x}} (r_{x,n|sz} \sigma_{sz|n} - \sigma_{sz|x}), \quad (\text{A12})$$

$$s_{x|n} = \frac{s_{sz|n}}{s_{sz|x}}, \quad (\text{A13})$$

We assume  $r_{x,n|sz} = 0$ . The scatter of  $Y_X - N$  relation is estimated using Eq. A14 of (Rozo et al. 2014a):

$$\sigma_{x|n}^2 = s_{x|m}^2 [\sigma_{m|n}^2 + \sigma_{m|x}^2 - 2r_{x,n|m} \sigma_{m|n} \sigma_{m|x}]. \quad (\text{A14})$$

The resultant  $\sigma_{x|n} = 0.69$  is very close to the  $\sigma_{sz|n} = 0.70$  (Rozo et al. 2014b; Table 4).

The binned  $Y_X$  presented as green bowties in Fig. 3 is  $\langle \ln Y_X | N \rangle$ , which is evaluated from  $\ln \langle Y_X | N \rangle - \frac{1}{2} \sigma_{x|n}^2$  assuming a log-normal distribution. When we present the expected  $Y_X$  inferred from *Planck* stacking  $Y_{SZ}$ , we include additional corrections listed as below. (1) From stacking  $\ln \langle Y_{SZ} | N \rangle$  (Planck Collaboration et al. 2011d; Table 1) to  $\langle \ln Y_{SZ} | N \rangle$ ,  $-\frac{1}{2} \sigma_{sz|n}^2 = -22\%$ . (2) Aperture-induced correction due to covariance, as the *Planck*  $Y_{SZ}$  is measured within  $R_{500}$ , which is based on maxBCG  $N_{200}$ . From Eq. A4 and replacing  $L_X$  with  $Y_{SZ}$ , the amplitude is over-biased with a factor of  $r_{sz,n|m} \beta s_{sz|m} \sigma_{m|sz} \sigma_{m|n}$  with  $r_{sz,n|m} = 0.47$  (Angulo et al. 2012), which is different from the case of  $Y_{SZ}$  measured from  $R_{500}$  independent of  $N_{200}$ . In that case,  $r_{sz,n|m}$  should be 0 or even negative, suggested by a negative hot gas - galaxy correlation when we derive the predicted multivariate scaling relation. The amplitude bias of  $r_{sz,n|m} \beta s_{sz|m} \sigma_{m|sz} \sigma_{m|n}$  is further divided by a factor of 2, as *Planck* measurements are template-amplitude fits rather than cylindrically integrated  $Y_{SZ}$  measurements and the inner radii weight more than the cylindrical integration. The final correction is  $-5\%$  (Rozo et al. 2014b). (3) Miscentering correction at a level of 10% in the richness range we present (Biesiadzinski et al. 2012). (4) Eddington bias correction based on Eq. A2, as we convert  $Y_{SZ}$  to  $Y_X$  using  $Y_{SZ} - Y_X$  relation (Rozo et al. 2014a; M10 data set in Table 1;  $\sigma_{x|sz} = \sigma_{sz|x} / s_{sz|x} = 0.15$ ) with a correction of  $-\beta \sigma_{x|sz}^2 = -6\%$ . (5) Aperture-induced correction due to hydrostatic or weak-lensing mass bias is ignored, because it is typically small relative with the mass bias itself.

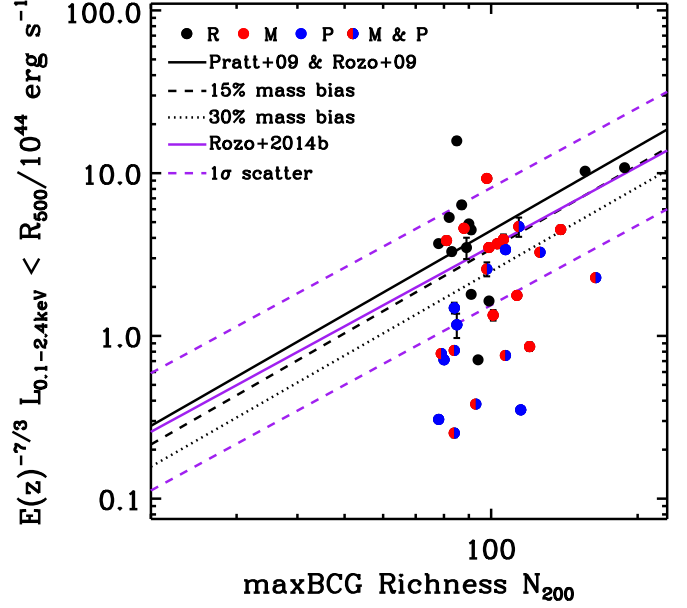


**Figure A2.** The same plot as Fig. 2, but for soft band 0.1-2.4 keV luminosity. The purple solid line with  $1\sigma$  dashed lines are from Rozo et al. (2014b).

## APPENDIX B: *Chandra* AND *XMM-Newton* CROSS-CALIBRATION

The X-ray data of our sample are from *Chandra* and *XMM-Newton*. There are some cross-calibration issues between these two instruments reported by the International Astronomical Consortium for High Energy Calibration (IACHEC, e.g., Schellenberger et al. 2015). We use six clusters in our sample with both the *Chandra* and *XMM-Newton* data and spanning a wide temperature range to do the in-house cross-calibration. We first measure the X-ray properties such as  $T_X$ ,  $L_X$  (bolometric), and  $Y_X$  individually from six clusters and independently from *Chandra* and *XMM-Newton*. All the X-ray properties are derived with the same procedures as detailed in Section 3. Note that  $R_{500}$  can be different for the *Chandra* data and the *XMM-Newton* data because of the different temperatures.

Fig. B1 compares the temperatures from *Chandra* and *XMM-Newton*, with *Chandra* temperatures systematically higher than *XMM-Newton*'s. We then fit the relation with a power-law function at  $T_X = 2 - 10.5$  keV as

$$\frac{kT_{XMM}}{1 \text{ keV}} = a_T \left( \frac{kT_{Ch}}{1 \text{ keV}} \right)^{s_T}, \quad a_T = 1.12 \pm 0.09, \quad s_T = 0.85 \pm 0.04. \quad (\text{B1})$$

Similarly, we have the power-law relations on  $L_X$  and  $Y_X$ :

$$\frac{L_{XMM}}{10^{44} \text{ erg s}^{-1}} = a_L \left( \frac{L_{Ch}}{10^{44} \text{ erg s}^{-1}} \right)^{s_L}, \quad a_L = 0.88 \pm 0.01, \quad s_L = 1.00 \pm 0.01. \quad (\text{B2})$$

$$\frac{Y_{XMM}}{10^{14} M_\odot \text{ keV}} = a_Y \left( \frac{Y_{Ch}}{10^{14} M_\odot \text{ keV}} \right)^{s_Y}, \quad a_Y = 0.86 \pm 0.04, \quad s_Y = 0.92 \pm 0.02. \quad (\text{B3})$$

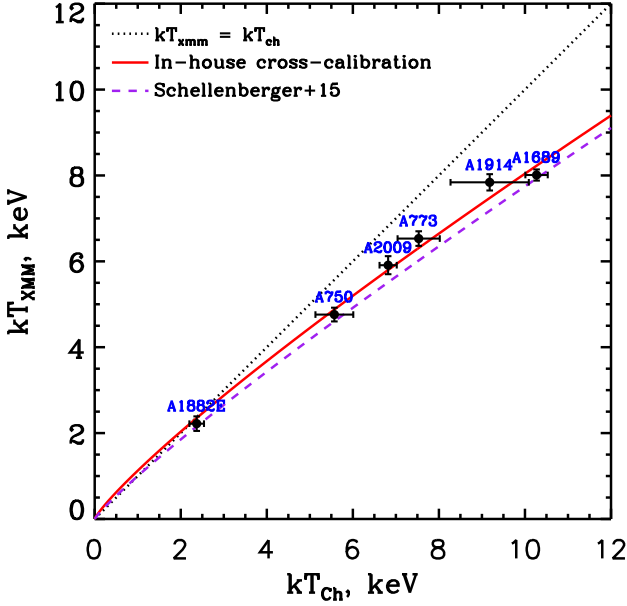


**Figure B1.** Comparison of temperatures from *Chandra* and *XMM-Newton* for six clusters in our sample. Temperatures are derived from 0.15–0.75  $R_{500}$  for *Chandra* and *XMM-Newton* respectively, with  $R_{500}$  determined iteratively from the  $M - T_X$  relation. The dotted line is the line of equality. The red line is our powerlaw best-fit relation (see Appendix B) used in this work, while the purple dashed line is from Schellenberger et al. (2015) ( $a_T = 1.00$  and  $s_T = 0.89$ ), with older *Chandra* and *XMM-Newton* calibrations than what we used.

## APPENDIX C: FEATURES OF INDIVIDUAL CLUSTERS

Here we briefly comment clusters in the sample, with emphasis on the substructure and dynamical state.

**A2142** is the richest maxBCG cluster. There is an ongoing merger as indicated by multiple cold fronts (Markevitch et al. 2000; Rossetti et al. 2013), radio halos (Venturi et al. 2017), and group-scale substructures (Owers et al. 2011). However, its global X-ray emission appears relaxed and both maxBCG and redMaPPer positions agree with each other.

**J150** is the 2nd richest maxBCG cluster. One may expect J150 as a massive ( $\sim 1.1 \times 10^{15} M_\odot$ ) and high temperature ( $kT \sim 10$  keV) cluster inferred from its optical richness. However from the *XMM* data, we find a  $\sim 5$  Mpc filament interlaced with three  $kT \sim 3$  keV clusters (J150E, J150M and J150W) and one group (J150EE;  $kT \sim 1.3$  keV). The maxBCG center is on J150E. redMaPPer identifies a cluster centered on J150W and a group on J150EE. However, the *Planck* SZ center is located at the X-ray brightest cluster (J150M). Thus this large-scale filament suffers problems of miscentering and projection when selected as a single optical cluster. Based on the mass derived from the X-ray temperature of different components, we estimate that the total maxBCG richness for three clusters and the group is 82 (vs. 164 from maxBCG), and the total redMaPPer richness for three clusters is 105.5 (vs. 151.4 from redMaPPer). Thus, this system is a particularly rich one in optical. Less X-ray luminous groups in this large-scale structure and projection contamination may also contribute.

**A1689** has a large concentration parameter and its gravitational lensing mass is higher than the X-ray mass by a factor of 2, which could be explained by its triaxial shape with the major axis nearly orientated along the line of sight (e.g., Morandi et al. 2011; Sereno et al. 2013; Umetsu et al. 2015). The triaxiality may be induced by a merger along the line of sight as indicated by the asymmetric temperature distribution (Andersson & Madejski 2004) and the diffuse radio emission (Vacca et al. 2011). However in the plane of sky, A1689 appears relaxed based on the X-ray morphology. The X-ray peak is also consistent with both maxBCG and redMaPPer centers.

**A1443** is a merging cluster from the X-ray E-W elongation and the diffuse radio emission (Bonafede et al. 2015). maxBCG and redMaPPer selected different galaxies as the BCG of the cluster.

**A781** in fact contains two large filaments projected on the sky, one  $\sim 2$  Mpc filament (A781, A781M, A781N;  $z \sim 0.29$ ) and another  $\sim 7$  Mpc filament (A781E, A781W;  $z \sim 0.43$ ). All these five clusters, including the X-ray faint A781N ( $kT = 1.3$  keV,  $L_X = 1.6 \times 10^{43}$  erg s $^{-1}$  in a  $2'$  radius), are confirmed by weak-lensing detections (Sehgal et al. 2008). A radio halo and a candidate radio relic was also discovered to be associated with the hottest cluster A781 (Govoni et al. 2011). maxBCG only detects the brightest A781, while redMaPPer detects A781E but mixes A781 with A781M.

**A1986** is not detected by *Planck*. The redMaPPer center is on the X-ray peak. The mass estimated from the redMaPPer richness ( $\sim 3.9 \times 10^{14} M_\odot$ ) is also consistent with the mass suggested by the X-ray temperature ( $\sim 3.2 \times 10^{14} M_\odot$ ). The maxBCG center is  $\sim 640$  kpc from the X-ray center and the maxBCG richness is biased high by  $\sim 2$ .

**A1882** is in a  $\sim 3$  Mpc filament at  $z \sim 0.14$  with at least four groups (A1882E, A1882M, A1882W, A1882N,  $kT \sim 1.3 - 2.3$  keV), which are corresponding to four concentrations of galaxy distribution (Owers et al. 2013). The merger is considered to be at an early stage from the large projected separation and the dearth of evidence for a recent major interaction in X-ray data (Owers et al. 2013). The maxBCG and redMaPPer centers are on A1882E and A1882W respectively. We estimate the corresponding optical richness from the total mass of the four groups derived from X-ray temperatures, 45 for maxBCG and 74 for redMaPPer, both lower than the richness values in the catalogs. There is also no *Planck* SZ detection in this region.

**A1758** is composed of A1758N and A1758S separated by  $\sim 2$  Mpc in projection with similar redshift ( $z \sim 0.28$ ) and X-ray luminosity. A1758N is in the late stage of a merger of two 7 keV subclusters near the plane of sky, while A1758S is in the early stage of a merger of two 5 keV subclusters close to the line of sight from detailed multi-wavelength observations (e.g., David & Kempner 2004; Giovannini et al. 2009; Durret et al. 2011; Monteiro-Oliveira et al. 2017). These two systems are most likely gravitationally bound and will eventually merge into a  $\sim 12$  keV cluster (David & Kempner 2004). The X-ray mass of A1758N and A1758S is  $8.9 \times 10^{14} M_\odot$  and  $5.7 \times 10^{14} M_\odot$  respectively, which can be compared with the masses suggested by their redMaPPer richness values ( $11.2 \times 10^{14} M_\odot$  for A1758N and  $2.7 \times 10^{14} M_\odot$  for A1758S). maxBCG only identifies A1758N with an optical mass of  $8.0 \times 10^{14} M_\odot$ .

**A1760** is divided into two clusters by redMaPPer and

the total richness of these two clusters is compatible with maxBCG's.

**A1622** is composed of two clusters as shown in the X-ray image. Only the X-ray properties of the northern one can be constrained from the shallow *Chandra* data. maxBCG and redMaPPer identified different galaxies as the BCG. Optical richness values from both maxBCG and redMaPPer suggest mass values of 2 - 3 times higher than the mass estimated from the X-ray temperature.

**A750** is composed of A750E/A750W at  $z \sim 0.16$ . A750W is possibly falling into A750E, as indicated by the highly disturbed X-ray morphology and the large offset of two X-ray peaks. Both maxBCG and redMaPPer mix these two clusters as one with different galaxies as the BCG. The X-ray masses of A750E and A750W are  $3.6 \times 10^{14} M_{\odot}$  and  $2.0 \times 10^{14} M_{\odot}$ , respectively, while the total mass estimated from the richness values of maxBCG and redMaPPer are 1.3 times and 2.4 times higher respectively.

**A1682** is a merging cluster as shown by the disturbed X-ray morphology. Both galaxy distribution and weak-lensing mass map show two peaks (Dahle et al. 2002) coincident with the X-ray peaks. The diffuse radio emission is complex with possible one halo and two relics (e.g., Macario et al. 2013). maxBCG and redMaPPer identified different galaxies as the BCG.

**A1246** has been observed to the virial radius with *Suzaku* (Sato et al. 2014). The X-ray mass within  $R_{500}$  ( $5.2 \times 10^{14} M_{\odot}$ ) from the  $M - T_X$  relation of the *Chandra* data is consistent with the mass derived from the *Suzaku* data ( $4.3 \times 10^{14} M_{\odot}$ ; Sato et al. 2014). maxBCG and redMaPPer identified different galaxies as the BCG.

**A1961** is a poor cluster ( $1.6 \times 10^{14} M_{\odot}$ ) from its X-ray temperature. However, the optical richness values from maxBCG and redMaPPer suggest mass values of 4 - 5 times higher. maxBCG and redMaPPer identified different galaxies as the BCG. The miscentering of maxBCG is large,  $\sim 1$  Mpc.

**A2034** is a merging cluster with the merger axis along S-N, as indicated by the northern shock (Owers et al. 2014) and the diffuse radio emission (Giovannini et al. 2009). The complex dynamics is also shown by the galaxy distribution (Owers et al. 2014) and weak-lensing mass distribution (Okabe & Umetsu 2008). The maxBCG and redMaPPer results are very similar.

**A655** hosts a dominated cD galaxy at the center, identified by both maxBCG and redMaPPer. However, the optical richness values from maxBCG and redMaPPer suggest mass values of  $\sim 3$  times higher than that from the X-ray temperature. The tentacle-like outskirts based on the X-ray morphology may suggest connection with other large-scale filaments and infalling galaxy groups as also suggested by Patej & Loeb 2016.

**A1914** is a merging cluster as indicated by two substructures along the NE-SW direction from the galaxy distribution (Barrena et al. 2013) and the weak-lensing mass distribution (Okabe & Umetsu 2008), as well as the diffuse radio emission (Bacchi et al. 2003). Both maxBCG and redMaPPer identified the same BCG, 175 kpc south to the X-ray peak.

**Z5247** is a merging cluster as indicated by the disturbed X-ray morphology. There are two X-ray peaks, corresponding to two substructures from the galaxy distribution and the

weak-lensing mass distribution (Dahle et al. 2002). The cluster also hosts a radio relic and a candidate radio halo (Kale et al. 2015). maxBCG and redMaPPer identified different galaxies as the BCG.

**A657** is not detected by *Planck*. While maxBCG and redMaPPer identified the same BCG close to the X-ray peak, the optical richness values from maxBCG and redMaPPer suggest mass values of 3 - 4 times higher than that from the X-ray temperature.

**J229** is a  $\sim 2.5$  keV system without *Planck* SZ detection. maxBCG and redMaPPer identified different galaxies as the BCG. The optical richness values from maxBCG and redMaPPer suggest mass values of 2 - 5 times higher than that from the X-ray temperature.

**A1423** is a relaxed cluster from the smooth X-ray morphology, galaxy distribution and weak-lensing mass distribution (Dahle et al. 2002).

**A801** appears relaxed in X-rays. The richness values from maxBCG and redMaPPer suggest a cluster mass similar to that derived from its X-ray temperature.

**A773** is a merging cluster as shown by evidence such as two X-ray peaks in the center along NE-SW, asymmetric X-ray temperature distribution (Govoni et al. 2004), two peaks of galaxy distribution and their velocity distribution (Barrena et al. 2007), two peaks in the weak-lensing mass distributions (Dahle et al. 2002), and diffuse radio emission (Govoni et al. 2001). The maxBCG mass ( $6.2 \times 10^{14} M_{\odot}$ ) matches with the X-ray mass ( $7.4 \times 10^{14} M_{\odot}$ ), while the redMaPPer mass ( $11.3 \times 10^{14} M_{\odot}$ ) is higher.

**A1576** is a disturbed cluster as indicated by its lopsided X-ray morphology and the presence of multiple peaks in galaxy distribution and weak-lensing mass distribution (Dahle et al. 2002).

**A2631** is classified as a disturbed cluster based on the multiple morphology parameters (Cassano et al. 2010). However, the weak-lensing map shows only one single peak (Okabe et al. 2010) and there is not any significant extended radio emission (Venturi et al. 2008).

**A1703** is a relaxed, unimodal cluster from the strong-lensing model (Richard et al. 2009). The maxBCG mass ( $6.0 \times 10^{14} M_{\odot}$ ) is close to X-ray mass ( $4.8 \times 10^{14} M_{\odot}$ ), while the redMaPPer mass ( $11.2 \times 10^{14} M_{\odot}$ ) is  $\sim 2$  times higher.

**A2219** is a merging cluster with the main merger axis along NW-SE direction, as shown by a series shocks and a possible cold front (Canning et al. 2017), two luminous BCGs in the cluster center and substructure in galaxy distribution (Boschin et al. 2004) and a diffuse radio halo (Bacchi et al. 2003). The redMaPPer mass ( $16.0 \times 10^{14} M_{\odot}$ ) is closed to the X-ray mass ( $13.3 \times 10^{14} M_{\odot}$ ), while the maxBCG mass ( $5.8 \times 10^{14} M_{\odot}$ ) is smaller.

**A1319** is composed of three clusters at similar redshifts, A1319M, A1319NW and A1319SW. Both maxBCG and redMaPPer only identified one cluster centered on the BCG of A1319M.

**A1560** is a merging cluster with two subclusters. The maxBCG center is on A1560SW and the redMaPPer center is on A1560NE.

**J175** is in a complex field with both foreground and background sources. X-ray emission mainly shows two clusters separated by  $\sim 2.5$  Mpc in projection along the N-S direction, J175N at  $z_{\text{spec}} = 0.117$  and J175S at  $z_{\text{spec}} = 0.119$ , which is also confirmed by redMaPPer. However, the maxBCG



cluster is centered on a luminous galaxy at  $z_{\text{spec}} = 0.117$ , nearly midway between J175N and J175S. The maxBCG center is very close to the foreground galaxy group HCG 58 (Hickson 1982; Freeland et al. 2009) that hosts the brightest X-ray source in the *XMM* field, the X-ray AGN of NGC 3822. The X-ray diffuse luminosity from this maxBCG region, excluding the NGC 3822 AGN, other point sources and diffuse emission from J175N/J175S is only  $\sim 3.3 \times 10^{42} \text{ erg s}^{-1}$  at the maxBCG cluster redshift. There is no *Planck* SZ source in this region. There is also a faint background cluster at  $z_{\text{spec}} = 0.280$ , detected by both maxBCG and redMaPPer.

**J249** is a cluster pair with comparable X-ray temperatures. There is no *Planck* SZ detection. maxBCG and redMaPPer identified different galaxies in J249SW as the BCG.

**A1201** is a merging cluster with the merger axis along NW-SE from the lopsided X-ray morphology. It hosts two cold fronts and an offset remnant core with a stripped tail (Ma et al. 2012). Substructures are identified from the spatial and velocity distribution of member galaxies (Owers et al. 2009). The strong-lensing arc indicates large mass elongation (Edge et al. 2003). maxBCG and redMaPPer identified different galaxies as the BCG.

**A2009** appears relaxed from the smooth X-ray morphology.

**A2111** is a merging cluster from the lopsided X-ray morphology and early X-ray observations (Wang et al. 1997; Henriksen et al. 1999). The member galaxy and weak-lensing mass distribution shows the same elongation as the X-rays in the NW-SE direction (Dahle et al. 2002). No significant diffuse radio emission has been detected (Venturi et al. 2008).

**A815** is a merging cluster from the disturbed X-ray morphology. A815N and A815S each has a luminous galaxy on its X-ray peak. There is no *Planck* SZ detection. There is a group to the east detected by the redMaPPer at a similar redshift. Based on the *XMM* data, we derive  $kT = 1.1 \text{ keV}$  and  $L_X = 1.5 \times 10^{43} \text{ erg s}^{-1}$  within  $R_{500}$  that is determined from redMaPPer's richness.

**Z1450** is a merging cluster from the asymmetric X-ray morphology. maxBCG and redMaPPer identified different galaxies as the BCG. The optical richness values from maxBCG and redMaPPer suggest mass values of 5 - 6 times higher than that from the X-ray temperature. There is no *Planck* SZ detection. There is a group to the SW at a similar redshift. The X-ray emission of this region is dominated by two bright point sources, which leaves insufficient amount of data to constrain the gas properties of this group.

**A1765** is a low mass ( $1.0 \times 10^{14} M_\odot$ ) cluster from the X-ray temperature ( $kT = 2.2 \text{ keV}$ ), while the optical richness values from maxBCG and redMaPPer suggest mass values of  $\sim 5$  times higher. There is no *Planck* SZ detection. There is a group to the east at a similar redshift. Based on the *XMM* data, we derive  $kT = 1.5 \text{ keV}$ ,  $L_X = 4.3 \times 10^{42} \text{ erg s}^{-1}$  within a  $1.5'$  radius.

**A1902** appears relaxed. Masses from optical and X-ray are consistent.

## APPENDIX D: LARGE-SCALE STRUCTURES

We also searched for large-scale structures around each maxBCG cluster in our sample, by looking at the maxBCG and redMaPPer catalogues, and examining *Chandra* and

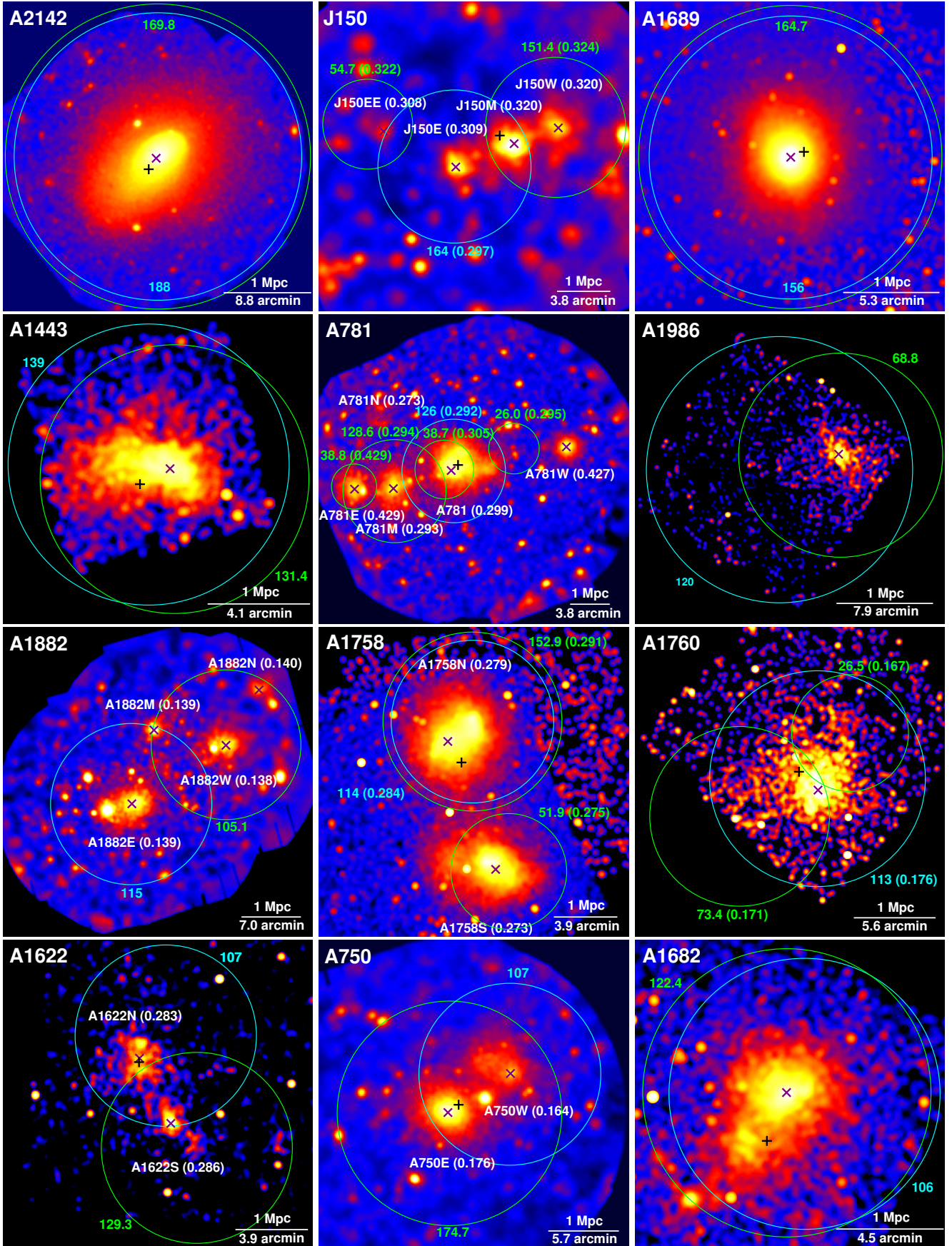
*XMM-Newton* data archives in a 1 degree radius (corresponding to  $\sim 13 \text{ Mpc}$  at  $z = 0.23$ ). Besides merging clusters like J150, A781, A1882 and A1319 as detailed in C, there are two additional large-scale structures, as shown in Fig. D1.

**J229-LS** contains at least four clusters (A2050, J229, A2051, A2051S;  $z \sim 0.12$ ) in a  $\sim 10 \text{ Mpc}$  filament. The X-ray properties of these clusters are also listed in Table 3. Note that A2051N is a background cluster at  $z \sim 0.38$ . Interestingly, the poor cluster J229 is identified as a rich optical cluster, while the hotter cluster A2051 is missed by both maxBCG and redMaPPer.

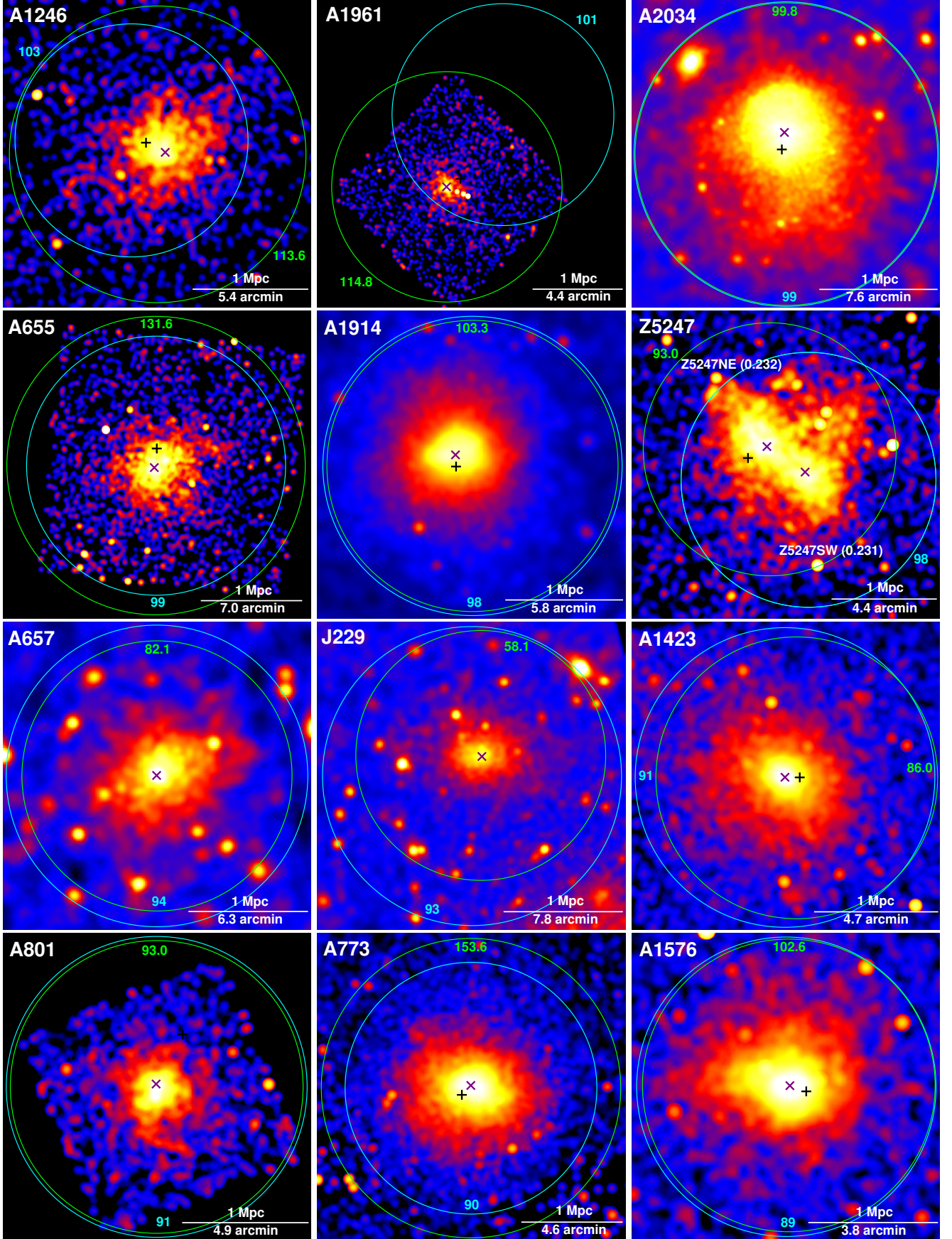
**A2219-LS** is composed of both A2219 and J249 in a  $\sim 6 \text{ Mpc}$  filament at  $z \sim 0.23$ . Both clusters are in this sample with similar maxBCG richness, while J249 is actually composed of two subclusters from the X-ray data.

## REFERENCES

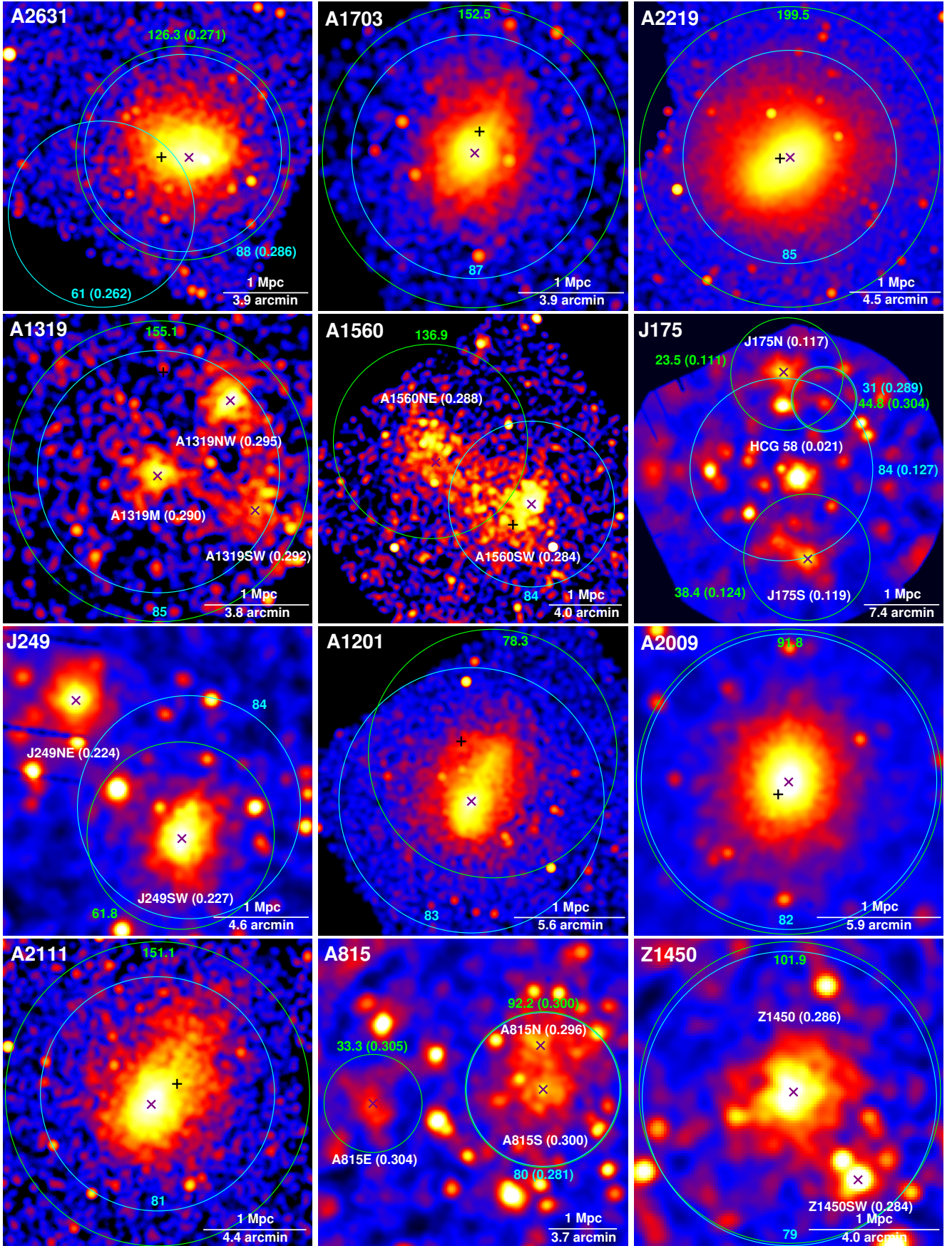
- Allen, S. W., Evrard, A. E., & Mantz, A. B. 2011, ARA&A, 49, 409
- Andersson, K. E., & Madejski, G. M. 2004, ApJ, 607, 190
- Andersson, K., Benson, B. A., Ade, P. A. R., et al. 2011, ApJ, 738, 48
- Andrade-Santos, F., Jones, C., Forman, W. R., et al. 2017, ApJ, 843, 76
- Andreoni, S., & Moretti, A. 2011, A&A, 536, A37
- Angulo, R. E., Springel, V., White, S. D. M., et al. 2012, MNRAS, 426, 2046
- Arnaud, K. A. 1996, Astronomical Data Analysis Software and Systems V, 101, 17
- Arnaud, M., Pointecouteau, E., & Pratt, G. W. 2007, A&A, 474, L37
- Arnaud, M., Pratt, G. W., Piffaretti, R., et al. 2010, A&A, 517, A92
- Asplund, M., Grevesse, N., Sauval, A. J., & Scott, P. 2009, ARA&A, 47, 481
- Bacchi, M., Feretti, L., Giovannini, G., & Govoni, F. 2003, A&A, 400, 465
- Barrena, R., Boschin, W., Girardi, M., & Spolaor, M. 2007, A&A, 467, 37
- Barrena, R., Girardi, M., & Boschin, W. 2013, MNRAS, 430, 3453
- Baxter, E. J., Raghunathan, S., Crawford, T. M., et al. 2018, MNRAS,
- Biesiadzinski, T., McMahon, J., Miller, C. J., Nord, B., & Shaw, L. 2012, ApJ, 757, 1
- Böhringer, H., Pratt, G. W., Arnaud, M., et al. 2010, A&A, 514, A32
- Bonafede, A., Intema, H., Brüggen, M., et al. 2015, MNRAS, 454, 3391
- Boschin, W., Girardi, M., Barrena, R., et al. 2004, A&A, 416, 839
- Bower, R. G., McCarthy, I. G., & Benson, A. J. 2008, MNRAS, 390, 1399
- Buote, D. A., Gastaldello, F., Humphrey, P. J., et al. 2007, ApJ, 664, 123
- Canning, R. E. A., Allen, S. W., Applegate, D. E., et al. 2017, MNRAS, 464, 2896
- Carlstrom, J. E., Holder, G. P., & Reese, E. D. 2002, ARA&A, 40, 643
- Cassano, R., Ettori, S., Giacintucci, S., et al. 2010, ApJ, 721, L82
- Corless, V. L., & King, L. J. 2007, MNRAS, 380, 149
- Croton, D. J., Springel, V., White, S. D. M., et al. 2006, MNRAS, 365, 11
- Dahle, H., Kaiser, N., Irgens, R. J., Lilje, P. B., & Maddox, S. J. 2002, ApJS, 139, 313
- Dai, X., Kochanek, C. S., & Morgan, N. D. 2007, ApJ, 658, 917











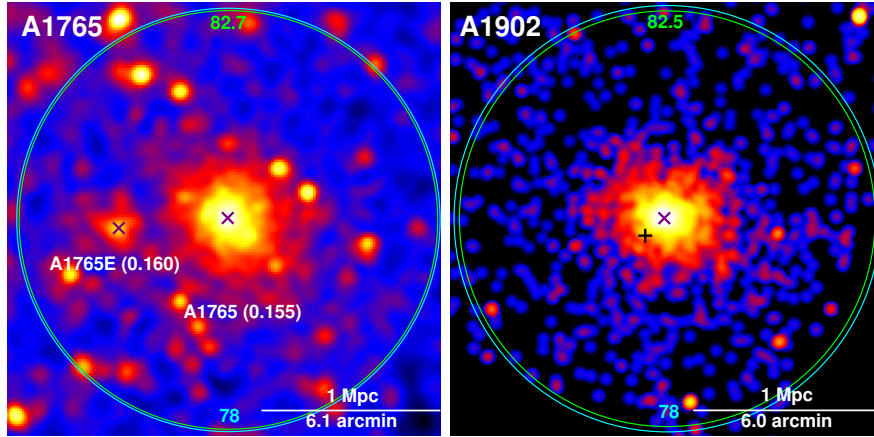


**Figure C1.** *Chandra* 0.7-2 keV/*XMM-Newton* 0.5-2 keV images of the 38 richest maxBCG clusters (in order of the maxBCG richness). All images are instrumental background subtracted, exposure corrected and smoothed. Purple  $\times$  marks the X-ray peak, while black  $+$  marks the SZ center from PSZ2 catalogue (Planck Collaboration et al. 2016). The centers of cyan and green circles are from the maxBCG (Koester et al. 2007) and redMaPPer (Rykoff et al. 2014) catalogue respectively, while the number marks the optical richness and the circles are  $R_{500}$  from the mass-richness relation (Rozo et al. 2009 for maxBCG and Simet et al. 2017 for redMaPPer). For multiple cluster systems, we also show the name and the spectroscopic redshift from *SDSS* for each X-ray cluster, as well as the photometric redshifts for the optical cluster from the optical catalogues.

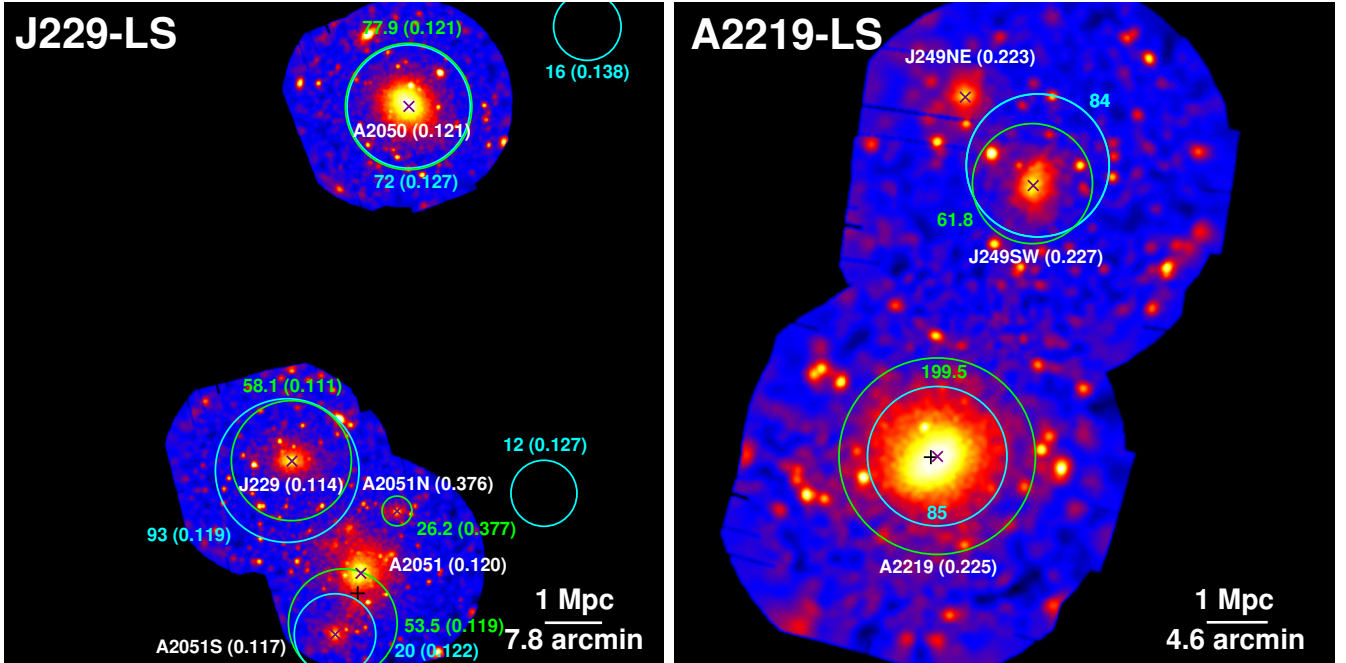


**Figure D1.** Large-scale structures identified around maxBCG clusters in our sample (the marks are the same as in Fig. C1).

David, L. P., & Kempner, J. 2004, *ApJ*, 613, 831  
Dietrich, J. P., Zhang, Y., Song, J., et al. 2014, *MNRAS*, 443, 1713  
Durret, F., Laganá, T. F., & Haider, M. 2011, *A&A*, 529, A38  
Edge, A. C., Smith, G. P., Sand, D. J., et al. 2003, *ApJ*, 599, L69  
Eke, V. R., Cole, S., Frenk, C. S., & Patrick Henry, J. 1998, *MNRAS*, 298, 1145  
Evrard, A. E., Arnault, P., Huterer, D., & Farahi, A. 2014, *MNRAS*, 441, 3562  
Farahi, A., Evrard, A. E., Rozo, E., Rykoff, E. S., & Wechsler, R. H. 2016, *MNRAS*, 460, 3900  
Farahi, A., Evrard, A. E., McCarthy, I., Barnes, D. J., & Kay,

S. T. 2017, arXiv:1711.04922  
Foster, A. R., Ji, L., Smith, R. K., & Brickhouse, N. S. 2012, *ApJ*, 756, 128  
Freeland, E., Stilp, A., & Wilcots, E. 2009, *AJ*, 138, 295  
Ge, C., Wang, Q. D., Tripp, T. M., et al. 2016, *MNRAS*, 459, 366  
Geach, J. E., & Peacock, J. A. 2017, *Nature Astronomy*, 1, 795  
Gilbank, D. G., Bower, R. G., Castander, F. J., & Ziegler, B. L. 2004, *MNRAS*, 348, 551  
Giovannini, G., Bonafede, A., Feretti, L., et al. 2009, *A&A*, 507, 1257  
Govoni, F., Feretti, L., Giovannini, G., et al. 2001, *A&A*, 376, 803  
Govoni, F., Markevitch, M., Vikhlinin, A., et al. 2004, *ApJ*, 605,



- 695
- Govoni, F., Murgia, M., Giovannini, G., Vacca, V., & Bonafede, A. 2011, *A&A*, 529, A69
- Gralla, M. B., Crichton, D., Marriage, T. A., et al. 2014, *MNRAS*, 445, 460
- Greco, J. P., Hill, J. C., Spergel, D. N., & Battaglia, N. 2015, *ApJ*, 808, 151
- Hand, N., Appel, J. W., Battaglia, N., et al. 2011, *ApJ*, 736, 39
- Henriksen, M., Wang, Q. D., & Ulmer, M. 1999, *MNRAS*, 307, 67
- Henry, J. P., & Arnaud, K. A. 1991, *ApJ*, 372, 410
- Hickson, P. 1982, *ApJ*, 255, 382
- Hinshaw, G., Larson, D., Komatsu, E., et al. 2013, *ApJS*, 208, 19
- Hudson, D. S., Mittal, R., Reiprich, T. H., et al. 2010, *A&A*, 513, A37
- Kaiser, N. 1986, *MNRAS*, 222, 323
- Kale, R., Venturi, T., Giacintucci, S., et al. 2015, *A&A*, 579, A92
- Koester, B. P., McKay, T. A., Annis, J., et al. 2007, *ApJ*, 660, 239
- Kravtsov, A. V., Nagai, D., & Vikhlinin, A. A. 2005, *ApJ*, 625, 588
- Kravtsov, A. V., Vikhlinin, A., & Nagai, D. 2006, *ApJ*, 650, 128
- Kuntz, K. D., & Snowden, S. L. 2008, *A&A*, 478, 575
- Lau, E. T., Kravtsov, A. V., & Nagai, D. 2009, *ApJ*, 705, 1129
- Lovisari, L., Forman, W. R., Jones, C., et al. 2017, *ApJ*, 846, 51
- Ma, C.-J., Owers, M., Nulsen, P. E. J., et al. 2012, *ApJ*, 752, 139
- Macario, G., Venturi, T., Intema, H. T., et al. 2013, *A&A*, 551, A141
- Mantz, A., Allen, S. W., Ebeling, H., Rapetti, D., & Drlica-Wagner, A. 2010, *MNRAS*, 406, 1773
- Mantz, A. B., Allen, S. W., Morris, R. G., et al. 2015, *MNRAS*, 449, 199
- Markevitch, M., Ponman, T. J., Nulsen, P. E. J., et al. 2000, *ApJ*, 541, 542
- Melin, J.-B., Bartlett, J. G., Delabrouille, J., et al. 2011, *A&A*, 525, A139
- Mohr, J. J., Fabricant, D. G., & Geller, M. J. 1993, *ApJ*, 413, 492
- Monteiro-Oliveira, R., Cypriano, E. S., Machado, R. E. G., et al. 2017, *MNRAS*, 466, 2614
- Morandi, A., Pedersen, K., & Limousin, M. 2011, *ApJ*, 729, 37
- Morandi, A., Sun, M., Forman, W., & Jones, C. 2015, *MNRAS*, 450, 2261
- Nagai, D., Kravtsov, A. V., & Vikhlinin, A. 2007, *ApJ*, 668, 1
- Navarro, J. F., Frenk, C. S., & White, S. D. M. 1997, *ApJ*, 490, 493
- Okabe, N., & Umetsu, K. 2008, *PASJ*, 60, 345
- Okabe, N., Takada, M., Umetsu, K., Futamase, T., & Smith, G. P. 2010, *PASJ*, 62, 811
- Owers, M. S., Nulsen, P. E. J., Couch, W. J., Markevitch, M., & Poole, G. B. 2009, *ApJ*, 692, 702
- Owers, M. S., Nulsen, P. E. J., & Couch, W. J. 2011, *ApJ*, 741, 122
- Owers, M. S., Baldry, I. K., Bauer, A. E., et al. 2013, *ApJ*, 772, 104
- Owers, M. S., Nulsen, P. E. J., Couch, W. J., et al. 2014, *ApJ*, 780, 163
- Patej, A., & Loeb, A. 2016, *ApJ*, 824, 69
- Planck Collaboration, Aghanim, N., Arnaud, M., et al. 2011, *A&A*, 536, A9
- Planck Collaboration, Aghanim, N., Arnaud, M., et al. 2011, *A&A*, 536, A10
- Planck Collaboration, Ade, P. A. R., Aghanim, N., et al. 2011, *A&A*, 536, A11
- Planck Collaboration, Aghanim, N., Arnaud, M., et al. 2011, *A&A*, 536, A12
- Planck Collaboration, Ade, P. A. R., Aghanim, N., et al. 2013, *A&A*, 557, A52
- Planck Collaboration, Ade, P. A. R., Aghanim, N., et al. 2016, *A&A*, 594, A27
- Pratt, G. W., Croston, J. H., Arnaud, M., & Böhringer, H. 2009, *A&A*, 498, 361
- Reiprich, T. H., & Böhringer, H. 2002, *ApJ*, 567, 716
- Richard, J., Pei, L., Limousin, M., Jullo, E., & Kneib, J. P. 2009, *A&A*, 498, 37
- Rossetti, M., Eckert, D., De Grandi, S., et al. 2013, *A&A*, 556, A44
- Rozo, E., Rykoff, E. S., Evrard, A., et al. 2009, *ApJ*, 699, 768
- Rozo, E., Wechsler, R. H., Rykoff, E. S., et al. 2010, *ApJ*, 708, 645
- Rozo, E., Evrard, A. E., Rykoff, E. S., & Bartlett, J. G. 2014, *MNRAS*, 438, 62
- Rozo, E., Bartlett, J. G., Evrard, A. E., & Rykoff, E. S. 2014, *MNRAS*, 438, 78
- Rozo, E., & Rykoff, E. S. 2014, *ApJ*, 783, 80
- Rykoff, E. S., McKay, T. A., Becker, M. R., et al. 2008, *ApJ*, 675, 1106-1124
- Rykoff, E. S., Rozo, E., Busha, M. T., et al. 2014, *ApJ*, 785, 104
- Santos, J. S., Rosati, P., Tozzi, P., et al. 2008, *A&A*, 483, 35
- Saro, A., Bocquet, S., Mohr, J., et al. 2017, *MNRAS*, 468, 3347
- Sato, K., Matsushita, K., Yamasaki, N. Y., Sasaki, S., & Ohashi, T. 2014, *PASJ*, 66, 85
- Schellenberger, G., Reiprich, T. H., Lovisari, L., Nevalainen, J., & David, L. 2015, *A&A*, 575, A30
- Sehgal, N., Hughes, J. P., Wittman, D., et al. 2008, *ApJ*, 673, 163-175
- Sehgal, N., Trac, H., Acquaviva, V., et al. 2011, *ApJ*, 732, 44
- Sehgal, N., Addison, G., Battaglia, N., et al. 2013, *ApJ*, 767, 38
- Serenio, M., Ettori, S., Umetsu, K., & Baldi, A. 2013, *MNRAS*, 428, 2241
- Simet, M., McClintock, T., Mandelbaum, R., et al. 2017, *MNRAS*, 466, 3103
- Snowden, S. L., Mushotzky, R. F., Kuntz, K. D., & Davis, D. S. 2008, *A&A*, 478, 615
- Sun, M., Voit, G. M., Donahue, M., et al. 2009, *ApJ*, 693, 1142
- Sun, M., Sehgal, N., Voit, G. M., et al. 2011, *ApJ*, 727, L49
- Sun, M. 2012, *New Journal of Physics*, 14, 045004
- Tinker, J., Kravtsov, A. V., Klypin, A., et al. 2008, *ApJ*, 688, 709-728
- Vacca, V., Govoni, F., Murgia, M., et al. 2011, *A&A*, 535, A82
- Umetsu, K., Sereno, M., Medezinski, E., et al. 2015, *ApJ*, 806, 207
- Venturi, T., Giacintucci, S., Dallacasa, D., et al. 2008, *A&A*, 484, 327
- Venturi, T., Rossetti, M., Brunetti, G., et al. 2017, *A&A*, 603, A125
- Vikhlinin, A., Burenin, R. A., Ebeling, H., et al. 2009, *ApJ*, 692, 1033
- Vikhlinin, A., Kravtsov, A. V., Burenin, R. A., et al. 2009, *ApJ*, 692, 1060
- Wang, Q. D., Ulmer, M. P., & Lavery, R. J. 1997, *MNRAS*, 288, 702
- Willingale, R., Starling, R. L. C., Beardmore, A. P., Tanvir, N. R., & O'Brien, P. T. 2013, *MNRAS*, 431, 394